Potent Neutralizing Antibodies Directed to Multiple Epitopes on SARS-CoV-2 Spike

Lihong Liu[1*], Pengfei Wang[1*], Manoj S. Nair[1*], Jian Yu[1*], Micah Rapp[2*], Qian Wang[3*], Yang Luo[1], Jasper F-W. Chan[4,5], Vincent Sahi[1], Amir Figueroa[6], Xinzheng V. Guo[7], Gabriele Cerutti[2], Jude Bimela[2], Jason Gorman[8], Tongqing Zhou[8], Zhiwei Chen[4,5,9], Kwok-Yung Yuen[4,5], Peter D. Kwong[8,10], Joseph G. Sodroski[3], Michael T. Yin[11], Zizhang Sheng[1,2], Yaoxing Huang[1#], Lawrence Shapiro[1,2,10#], and David D. Ho[1#]

[1]Aaron Diamond AIDS Research Center, Columbia University Vagelos College of Physicians and Surgeons, New York, NY 10032, USA.

[2]Zuckerman Mind Brain Behavior Institute, Columbia University, New York, NY 10027, USA.

[3]Dana-Farber Cancer Institute, Harvard Medical School, Boston, MA 02215, USA.

[4]State Key Laboratory of Emerging Infectious Diseases, Carol Yu Centre for Infection, Department of Microbiology, Li Ka Shing Faculty of Medicine, The University of Hong Kong, Hong Kong Special Administrative Region, China.

[5]Centre for Virology, Vaccinology and Therapeutics, Health@InnoHK, The University of Hong Kong, Hong Kong Special Administrative Region, China.

[6]Department of Microbiology & Immunology Flow Cytometry Core, Columbia University Vagelos College of Physicians and Surgeons, New York, NY 10032, USA.

[7]Human Immune Monitoring Core, Columbia University Vagelos College of Physicians and Surgeons, New York, NY 10032, USA.

[8]Vaccine Research Center, National Institutes of Health, Bethesda, MD 20892, USA.

23 [9]AIDS Institute, Li Ka Shing Faculty of Medicine, The University of Hong Kong, Hong Kong
24 Special Administrative Region, China.
25 [10]Department of Biochemistry, Columbia University, New York, NY 10032, USA.
26 [11]Division of Infectious Diseases, Department of Internal Medicine, Columbia University
27 Vagelos College of Physicians and Surgeons, New York, NY 10032, USA.
28 [*]Equal contribution.
29 # Address correspondence to David D. Ho: dh2994@cumc.columbia.edu; Lawrence Shapiro:
30 lss8@columbia.edu; Yaoxing Huang: yh3253@cumc.columbia.edu.

Abstract

The SARS-CoV-2 pandemic rages on with devasting consequences on human lives and the global economy[1,2]. The discovery and development of virus-neutralizing monoclonal antibodies could be one approach to treat or prevent infection by this novel coronavirus. Here we report the isolation of 61 SARS-CoV-2-neutralizing monoclonal antibodies from 5 infected patients hospitalized with severe disease. Among these are 19 antibodies that potently neutralized the authentic SARS-CoV-2 *in vitro*, 9 of which exhibited exquisite potency, with 50% virus-inhibitory concentrations of 0.7 to 9 ng/mL. Epitope mapping showed this collection of 19 antibodies to be about equally divided between those directed to the receptor-binding domain (RBD) and those to the N-terminal domain (NTD), indicating that both of these regions at the top of the viral spike are immunogenic. In addition, two other powerful neutralizing antibodies recognized quaternary epitopes that are overlapping with the domains at the top of the spike. Cryo-electron microscopy reconstructions of one antibody targeting RBD, a second targeting NTD, and a third bridging two separate RBDs revealed recognition of the closed, "all RBD-down" conformation of the spike. Several of these monoclonal antibodies are promising candidates for clinical development as potential therapeutic and/or prophylactic agents against SARS-CoV-2.

Background

A novel coronavirus, now termed SARS-CoV-2[1,2], has caused over 11 million confirmed infections globally, leading to over 500,000 deaths. This pandemic has also put much of the world on pause, with unprecedented disruption of lives and unparalleled damage to the economy. A return to some semblance of normalcy will depend on science to deliver an effective solution, and

54 the scientific community has responded admirably. Drug development is well underway, and
55 vaccine candidates have entered clinical trials. Another promising approach is the isolation of
56 SARS-CoV-2-neutralizing monoclonal antibodies (mAbs) that could be used as therapeutic or
57 prophylactic agents. The primary target for such antibodies is the viral spike, a trimeric protein[3,4]
58 that is responsible for binding to the ACE2 receptor on the host cell[1,3,5,6]. The spike protein is
59 comprised of two subunits. The S1 subunit has two major structural elements: RBD and NTD; the
60 S2 subunit mediates virus-cell membrane fusion after the RBD engages ACE2. Reports of
61 discovery of neutralizing mAbs that target the RBD have been published recently[7-11]. We now
62 describe our efforts in isolating and characterizing a collection of mAbs that not only target
63 multiple epitopes on the viral spike but also show exquisite potency in neutralizing SARS-CoV-2.
64

65 **Patient Selection**

66 Forty patients with PCR-confirmed SARS-CoV-2 infection were enrolled in a cohort study on
67 virus-neutralizing antibodies. Plasma samples from all subjects were first tested for neutralizing
68 activity against SARS-CoV-2 pseudovirus (Wuhan-Hu-1 spike pseudotyped with vesicular
69 stomatitis virus). Widely varying neutralizing titers were observed, with IC_{50} ranging from a
70 reciprocal plasma dilution of <100 to ~13,000 (Fig. 1a). Five patients were chosen for mAb
71 isolation because their plasma virus-neutralizing titers were among the highest. The clinical
72 characteristics of these 5 cases are summarized in Extended Data Table 1. All were severely ill
73 with acute respiratory distress syndrome requiring mechanical ventilation.
74

75 **Monoclonal Antibody Isolation and Construction**

76 Peripheral blood mononuclear cells from each patient were put through an experimental schema
77 (Extended Data Fig. 1a) starting with cell sorting by flow cytometry. The sorting strategy focused
78 on live memory B lymphocytes that were CD3-negative, CD19-positive, and CD27-positive
79 (Extended Data Fig. 1b). The final step focused on those cells that bound the SARS-CoV-2 spike
80 trimer (S trimer)[4]. A total of 602, 325, 14, 147, and 145 such B cells from Patient 1, Patient 2,
81 Patient 3, Patient 4, and Patient 5, respectively, were labelled with a unique hashtag (Extended
82 Data Fig. 1c). The cells were then placed into the 10X Chromium (10X Genomics) for single-cell
83 5'mRNA and V(D)J sequencing to obtain paired heavy (H) and light (L) chain sequences. A
84 careful bioinformatic analysis was carried out on 1,145 paired sequences to downselect "high-
85 confidence" antigen-specific mAbs. A total of 331 mAb sequences were recovered, representing
86 252 individual clones. Only 6 mAbs were from Patient 3, whereas 44 to 100 mAbs were identified
87 from each of the other patients (Extended Data Table 2). The VH and VL sequences of 252
88 antibodies (one per clone) were codon-optimized and synthesized, and each VH and VL gene was
89 then cloned into an expression plasmid with corresponding constant region of H chain and L chain
90 of human IgG1, and mAbs were expressed by co-transfection of paired full-length H chain and L
91 chain genes into Expi293 cells.
92
93 **Monoclonal Antibody Screening**
94 All 252 transfection supernatants were screened for binding to S trimer and RBD by enzyme-
95 linked immunosorbent assays (ELISAs), as well as for neutralization against SARS-CoV-2
96 pseudovirus and live virus. These results are graphically represented in Fig. 1b and tabulated in
97 Extended Data Table 2. It was evident that a substantial percentage of the mAbs in the supernatants
98 bound S trimer, and a subset of those bound RBD. Specifically, 121 supernatants were scored as

99 positive for S trimer binding, yielding an overall hit rate of 48%. Of these, 38 were positive for
100 RBD binding while the remaining 83 were negative. None of the 13 trimer-specific mAbs from
101 Patient 5 recognized RBD. In the pseudovirus neutralization screen, 61 supernatants were scored
102 as positive, indicating that half of the trimer-specific mAbs were virus neutralizing. In the screen
103 for neutralization against SARS-CoV-2 (strain USA-WA1/2020), 41 supernatants were scored as
104 positive. Overall, this screening strategy was quite effective in picking up neutralizing mAbs
105 (vertical lines and labelled antibodies at the bottom of Fig. 1b) that were later identified as potent.
106

107 **Sequence Analysis of S Trimer-Specific Monoclonal Antibodies**

108 Of the 121 mAbs that bound S trimer, 88% were IgG isotype, with IgG1 being predominant
109 (Extended Data Fig. 2a). Comparison to the IgG repertoire of three healthy human donors[12]
110 revealed a statistically significant over-representation of IGHV3-30, IGKV3-20, and IGHJ6 genes
111 for this collection of SARS-CoV-2 mAbs (Extended Data Figs. 2b and 2c). A longer average
112 CDRH3 length was also noted (Extended Data Fig. 2d). Interestingly, the average percentages of
113 somatic hypermutation in VH and VL were 2.1 and 2.5, respectively, which were significantly
114 lower than those found in healthy individuals (Extended Data Fig. 2e) and remarkably close to
115 germline sequences.
116

117 **Antigen Binding and Virus Neutralization**

118 Since the screening for pseudovirus neutralization was performed quantitatively with serial
119 dilutions of the transfection supernatants, we plotted in Extended Data Fig. 3 the best-fit
120 neutralization curves for 130 samples that were positive in at least one of the screens shown in Fig.
121 1b. Most were non-neutralizing or weakly neutralizing, but 18 showed evidently better potency.

122 One additional supernatant was initially missed in the pseudovirus screen (Patient 1 in Extended
123 Data Fig. 3) but was later found to be a potent neutralizing mAb. Together, these 19 mAbs were
124 purified from transfection supernatants and further characterized for their binding and
125 neutralization properties. As shown in Fig. 2a, all but one (2-43) of the mAbs bound the S trimer
126 by a quantitative ELISA. Nine of the antibodies clearly bound RBD, with little or no binding to
127 NTD. Eight antibodies bound NTD to varying degrees, with no binding to RBD. Two mAbs
128 bound neither RBD nor NTD, and were therefore categorized as "Others".
129
130 The pseudovirus neutralization profiles for these purified 19 mAbs are shown in the top portion of
131 Fig. 2b. The RBD-directed antibodies neutralized the pseudovirus with IC_{50} of 0.005 to 0.512
132 μg/mL; the NTD-directed antibodies were slightly less potent, with IC_{50} ranging from 0.013 to
133 0.767 μg/mL. A common feature of the NTD mAbs was the plateauing of virus neutralization at
134 levels short of 100%. Two antibodies, categorized as "Others", neutralized with IC_{50} of 0.071 and
135 0.652 μg/mL. Antibody neutralization of the authentic or live SARS-CoV-2 (strain USA-
136 WA1/2020) was carried out using Vero cells inoculated with a multiplicity of infection of 0.1. As
137 shown in the bottom portion of Fig. 2b, the RBD-directed antibodies again neutralized the virus
138 but with IC_{50} of 0.0007 to 0.209 μg/mL; the NTD-directed antibodies showed similar potency,
139 with IC_{50} ranging from 0.007 to 0.109 μg/mL. Here, the plateauing effect seen in the pseudovirus
140 neutralization assay was less apparent. Antibodies 2-43 and 2-51 neutralized the live virus with
141 IC_{50} of 0.003 and 0.007 μg/mL, respectively. Overall, nine mAbs exhibited exquisite potency in
142 neutralizing authentic SARS-CoV-2 *in vitro* with IC_{50} of 0.009 μg/mL or less, including four
143 directed to RBD (2-15, 2-7, 1-57, and 1-20), three to NTD (2-17, 5-24, and 4-8), and two to
144 undetermined regions on the S trimer (2-43 and 2-51). It is remarkable that Patient 2 alone

145 contributed five of the top nine SARS-CoV-2 neutralizing mAbs. Correlation of the results of the
146 two virus-neutralizing assays is shown in Extended Data Fig. 4.
147
148 **Epitope Mapping**
149 All 19 potent neutralizing mAbs (Fig. 2) were further studied in antibody competition experiments
150 to gain insight into their epitopes. In addition, 12 mAbs that bound the S trimer strongly during
151 the initial supernatant screen were also chosen, including 5 that bound RBD (1-97, 2-26, 4-13, 4-
152 24, and 4-29) and 7 that did not bind RBD (1-21, 2-29, 4-15, 4-32, 4-33, 4-41, and 5-45). Four of
153 these mAbs were weak in neutralizing SARS-CoV-2 pseudovirus, and the remaining 8 were non-
154 neutralizing (Extended Data Fig. 5). First, a total of 16 non-RBD mAbs were evaluated for
155 competition in binding to S trimer by ELISA in a "checkerboard" experiment. The extent of the
156 antibody competition is reflected by the intensity of the heatmap shown in Fig. 3a. There is one
157 large cluster (A) of mAbs that competed with one another, and it partially overlaps a small cluster
158 (B). A third cluster (C) does not overlap at all. Note that all but one of the antibodies in cluster A
159 recognized NTD. Antibody 2-51 is clearly directed to the NTD region even though it could not
160 bind NTD. Moreover, one mAb each from clusters B and C also recognized NTD, thereby
161 indicating that all three clusters are within or near the NTD. One mAb, 1-21, appears to have a
162 unique non-overlapping epitope (epitope region D).
163
164 Second, a similar "checkerboard" competition experiment was carried out by ELISA for 14 of our
165 RBD-directed mAbs plus CR3022[13,14]. Here, the heatmap shows that there are four epitope
166 clusters that are serially overlapping (Fig. 3a). There is one large cluster (E) that contains mAbs
167 largely capable of blocking ACE2 binding. Furthermore, 4 antibodies in this cluster lost binding

168 to a mutant RBD (L455R, A475R, G502R) that could no longer bind ACE2 (our unpublished
169 findings). Taken together, these results suggest that most of the mAbs in cluster E are directed to
170 the ACE2-binding interface of RBD. The next cluster (F) connects to both cluster E and cluster
171 G, the location of which is defined by its member CR3022[15]. Lastly, cluster G overlaps another
172 cluster (H), which includes 1-97 that strongly inhibited the binding of 2-30 to the S trimer. This
173 finding suggests that cluster H may be proximal to one edge of cluster E.
174
175 One potent neutralizing mAb, 2-43, did not bind S trimer by ELISA (Fig. 2a) and thus could not
176 be tested in the above competition experiments. However, 2-43 did strongly bind S trimer when
177 expressed on the cell surface as determined by flow cytometry (Extended Data Fig. 6a), and this
178 binding was competed out by itself but not by RBD, NTD, ACE2, or the soluble S trimer[4]
179 (Extended Data Fig. 6b). NTD-directed mAbs had only a modest effect on its binding to cell-
180 surface S trimer, but numerous RBD-directed mAbs in cluster E potently blocked the binding of
181 2-43, demonstrating that this antibody is likely targeting a quaternary epitope on the top of RBD.
182
183 These mapping results could be represented by two sets of Venn diagrams shown in Fig. 3b. In
184 the non-RBD region, the potent neutralizing mAbs reside exclusively in cluster A and bind a patch
185 on the NTD. Weaker neutralizing mAbs recognize a region at the interface between clusters A
186 and B. In the RBD region, the most potent neutralizing mAbs also group together within one
187 cluster (E). Given that all block ACE2 binding, it is likely they recognize the top of RBD and
188 neutralize the virus by competitive inhibition of receptor binding. Cluster G contains CR3022, a
189 mAb known to be directed to an epitope on a cryptic site on the side of RBD when it is in the "up"
190 position[15]. Cluster F is therefore likely situated between the top and this "cryptic" site. The Venn

191 diagram also suggests that cluster H may occupy a different side surface of RBD, perhaps in the
192 region recognized by S309, a mAb isolated from a SARS-CoV-1 patient[8].
193
194 **Cryo-Electron Microscopy**
195 We produced cryo-EM reconstructions of Fabs from three mAbs in complex with the S trimer[4].
196 First, single-particle analysis of the complex with 2-4 Fab (RBD-directed) yielded maps of high
197 quality (Fig. 4a; Extended Data Table 3; Extended Data Fig. 7), with the most abundant particle
198 class representing a 3-Fab-per-trimer complex, refined to an overall resolution of 3.2 Å. While
199 density for the constant portion of the Fabs was visible, it was blurred due to molecular motion,
200 and thus only the variable domains were included in the molecular model. Fab 2-4 bound the spike
201 protein near the apex, with all RBDs in the "down" orientation, and the structure of the antibody-
202 bound spike protein was highly similar to previously published unliganded spike structures in the
203 "all-down" conformation[3,4]. Detailed interactions between 2-4 and RBD are discussed and
204 exhibited in Extended Data Fig. 8. Overall, the structure of the 2-4 Fab-spike complex shows that
205 neutralization of SARS-CoV-2 by this mAb likely results from locking RBD in the down
206 conformation while also occluding access to ACE2.
207
208 Second, we also produced 3D cryo-EM reconstructions of 4-8 Fab (NTD-directed) in complex
209 with the S trimer (Extended Data Table 3; Extended Data Fig. 9). Two main particle classes were
210 observed – one for a 3-Fab-bound complex with all RBDs "down" at 3.9 Å resolution (Fig. 4b),
211 and another a 3-Fab-bound complex with one RBD "up" at 4.0 Å resolution (Extended Data Fig.
212 10). However, molecular motion prevented visualization of the interaction at high resolution.
213 Nevertheless, the density in the 4-8 map reveals the overall positions of the antibody chains

214 targeting NTD. Such binding to the tip of NTD results in SARS-CoV-2 neutralization remains
215 unclear.
216
217 Third, a 5.8 Å resolution reconstructions of 2-43 Fab in complex with the S trimer (Extended Data
218 Table 3; Extended Data Fig. 11) revealed three bound Fabs, each targeting a quaternary epitope
219 on the top of the spike that included elements of the RBDs from two adjacent S1 protomers (Fig.
220 4c), consistent with the epitope mapping results (Extended Data Fig. 6b and Fig. 3b), including
221 the lack of binding to isolated RBD (Fig. 2a). Given these findings, the inability of 2-43 to bind S
222 trimer by ELISA is likely an artifact of the assay format, as this mAb did bind the spike expressed
223 on the cell surface and in the cryo-EM study.
224
225 Armed with these three cryo-EM reconstructions, we used the Venn diagrams from Fig. 3b to map
226 the epitopes of many of our SARS-CoV-2 neutralizing mAbs onto the surface of the spike (Fig.
227 4d). This is obviously a rough approximation since antibody footprints are much larger than the
228 area occupied by the mAb number. However, the spatial relationship of the antibody epitopes
229 should be reasonably represented by Fig. 4d.
230
231 **Protection of Hamsters from SARS-CoV-2 Infection by mAb 2-15**
232 To assess the *in vivo* potency of mAb 2-15, we performed a protection experiment in a golden
233 Syrian hamster model of SARS-CoV-2 infection. The hamsters were first given an intraperitoneal
234 injection of the antibody at a dose of 1.5 mg/kg or 0.3 mg/kg, or PBS alone. Intranasal inoculations
235 of 10^5 plaque-forming units (PFU) of the HKU-001a strain of SARS-CoV-2 were carried out 24
236 hours later. Four days after virus challenge, lung tissues were harvested to quantify the viral load.

237 As shown in Fig. 5, both viral RNA copy numbers and infectious virus titers were reduced by 4
238 logs or more in hamsters given the dose of 1.5 mg/kg of mAb 2-15. The protection at the dose of
239 0.3 mg/kg was borderline, as we had estimated. This pilot animal study demonstrates that the
240 potency of mAb 2-15 *in vitro* is indeed reflected *in vivo*, with complete elimination of infectious
241 SARS-CoV-2 at a relatively modest antibody dose.
242
243 **Discussion**
244 We have discovered a collection of SARS-CoV-2-neutralizing mAbs that are not only potent but
245 also diverse. Nine of these antibodies can neutralize the authentic virus *in vitro* at concentrations
246 of 9 ng/mL or less (Fig. 2b), including 4 directed to RBD, 3 directed to NTD, and 2 to quaternary
247 epitopes nearby. Surprisingly, many of the these mAbs have V(D)J sequences close to germline
248 sequences, without extensive somatic hypermutations (Extended Data Fig. 2e), a finding that bodes
249 well for vaccine development. Our most potent RBD-specific mAbs (e.g., 2-15, 2-7, 1-57, and 1-
250 20) compare favorably with such antibodies recently reported[7,8,10,16-20], including those with high
251 potency[9,11,21,22]. The *in vitro* potency of 2-15 is well reflected *in vivo* in the hamster protection
252 experiment (Fig. 5). It appears from the epitope mapping studies that mAbs directed to the top of
253 RBD strongly compete with ACE2 binding and potently neutralize the virus, whereas those
254 directed to the side surfaces of RBD do not compete with ACE2 and neutralize less potently (Figs.
255 3b and 4d). Our collection of non-RBD neutralizing mAbs is unprecedented in that such antibodies
256 only have been sporadically reported and only with substantially lower potencies[22-24]. The most
257 potent of these mAbs are directed to (e.g., 2-17, 5-24, and 4-8) or overlapping with (2-51) a patch
258 on the NTD (Figs. 3b and 4d). It is unclear how NTD-directed mAbs block SARS-CoV-2 infection
259 and why their neutralization profiles are different from those of RBD-directed antibodies (Fig. 2b).

260 Nevertheless, vaccine strategies that do not include NTD will be unable to induce an important
261 class of virus-neutralizing antibodies.
262
263 The isolation of two mAbs (2-43 and 2-51) directed to epitopes that do not map to RBD and NTD
264 is also unprecedented. Cryo-EM of 2-43 Fab bound to the S trimer has confirmed its epitope as
265 quaternary in nature, crossing from the top of one RBD to the top of another RBD (Fig. 4c). It
266 will be equally informative to understand the epitope of 2-51. In this study, we also show the first
267 evidence by cryo-EM for a neutralizing mAb (4-8) bound to the NTD of the viral spike (Fig. 4b),
268 as well as another high-resolution structure of a mAb (2-4) bound to RBD (Fig. 4a).
269
270 The potency and diversity of our SARS-CoV-2-neutralizing mAbs are likely attributable to patient
271 selection. Previously, we observed that infected individuals with severe disease developed a more
272 robust virus-neutralizing antibody response[25]. If Patient 2 had not been included, five of the top
273 neutralizing mAbs would be lost. The diversity of our antibodies is also attributable, in part, to
274 the choice of using the S trimer to sort from memory B cells, while most groups focused on the
275 use of RBD[7,9-11,16-19,21]. The characterization of this diverse collection of mAbs has allowed us to
276 observe that all potent SARS-CoV-2-neutralizing antibodies described to date are directed to the
277 top of the viral spike. RBD and NTD are, no doubt, quite immunogenic. Neutralizing antibodies
278 to the stem region of the S trimer remain to be discovered. In conclusion, we believe several of
279 our monoclonal antibodies with exquisite virus-neutralizing activity are promising candidates for
280 development as modalities to treat or prevent SARS-CoV-2 infection.

References

1 Zhou, P. *et al.* A pneumonia outbreak associated with a new coronavirus of probable bat origin. *Nature* **579**, 270-273, doi:10.1038/s41586-020-2012-7 (2020).

2 Wang, C., Horby, P. W., Hayden, F. G. & Gao, G. F. A novel coronavirus outbreak of global health concern. *Lancet* **395**, 470-473, doi:10.1016/S0140-6736(20)30185-9 (2020).

3 Walls, A. C. *et al.* Structure, Function, and Antigenicity of the SARS-CoV-2 Spike Glycoprotein. *Cell* **181**, 281-292 e286, doi:10.1016/j.cell.2020.02.058 (2020).

4 Wrapp, D. *et al.* Cryo-EM structure of the 2019-nCoV spike in the prefusion conformation. *Science* **367**, 1260-1263, doi:10.1126/science.abb2507 (2020).

5 Hoffmann, M. *et al.* SARS-CoV-2 Cell Entry Depends on ACE2 and TMPRSS2 and Is Blocked by a Clinically Proven Protease Inhibitor. *Cell* **181**, 271-280 e278, doi:10.1016/j.cell.2020.02.052 (2020).

6 Wang, Q. *et al.* Structural and Functional Basis of SARS-CoV-2 Entry by Using Human ACE2. *Cell* **181**, 894-904 e899, doi:10.1016/j.cell.2020.03.045 (2020).

7 Ju, B. *et al.* Human neutralizing antibodies elicited by SARS-CoV-2 infection. *Nature*, doi:10.1038/s41586-020-2380-z (2020).

8 Pinto, D. *et al.* Cross-neutralization of SARS-CoV-2 by a human monoclonal SARS-CoV antibody. *Nature*, doi:10.1038/s41586-020-2349-y (2020).

9 Cao, Y. *et al.* Potent neutralizing antibodies against SARS-CoV-2 identified by high-throughput single-cell sequencing of convalescent patients' B cells. *Cell*, doi:10.1016/j.cell.2020.05.025 (2020).

10 Wu, Y. *et al.* A noncompeting pair of human neutralizing antibodies block COVID-19 virus binding to its receptor ACE2. *Science* **368**, 1274-1278, doi:10.1126/science.abc2241 (2020).

11 Hansen, J. *et al.* High-Throughput Effort Using Both Humanized Mice and Convalescent Humans Yields SARS-CoV-2 Antibody Cocktail. *Science*, doi:in press (2020).

12 Sheng, Z. *et al.* Gene-Specific Substitution Profiles Describe the Types and Frequencies of Amino Acid Changes during Antibody Somatic Hypermutation. *Front Immunol* **8**, 537, doi:10.3389/fimmu.2017.00537 (2017).

13 ter Meulen, J. *et al.* Human monoclonal antibody combination against SARS coronavirus: synergy and coverage of escape mutants. *Plos Med* **3**, e237, doi:10.1371/journal.pmed.0030237 (2006).

14 Tian, X. *et al.* Potent binding of 2019 novel coronavirus spike protein by a SARS coronavirus-specific human monoclonal antibody. *Emerg Microbes Infect* **9**, 382-385, doi:10.1080/22221751.2020.1729069 (2020).

15 Yuan, M. *et al.* A highly conserved cryptic epitope in the receptor binding domains of SARS-CoV-2 and SARS-CoV. *Science* **368**, 630-633, doi:10.1126/science.abb7269 (2020).

16 Rogers, T. F. *et al.* Rapid isolation of potent SARS-CoV-2 neutralizing antibodies and protection in a small animal model. *bioRxiv*, doi:10.1101/2020.05.11.088674 (2020).

17 Chen, X. *et al.* Human monoclonal antibodies block the binding of SARS-CoV-2 spike protein to angiotensin converting enzyme 2 receptor. *Cell Mol Immunol* **17**, 647-649, doi:10.1038/s41423-020-0426-7 (2020).

18 Zeng, X. *et al.* Isolation of a human monoclonal antibody specific for the receptor binding domain of SARS-CoV-2 using a competitive phage biopanning strategy. *Antibody Therapeutics* **3**, 95-100, doi:10.1093/abt/tbaa008 (2020).

19 Liu, X. *et al.* Neutralizing Antibodies Isolated by a site-directed Screening have Potent Protection on SARS-CoV-2 Infection. *bioRxiv*, 2020.2005.2003.074914, doi:10.1101/2020.05.03.074914 (2020).

20 Zost, S. J. *et al.* Rapid isolation and profiling of a diverse panel of human monoclonal antibodies targeting the SARS-CoV-2 spike protein. *bioRxiv*, doi:10.1101/2020.05.12.091462 (2020).

21 Robbiani, D. F. *et al.* Convergent Antibody Responses to SARS-CoV-2 Infection in Convalescent Individuals. *bioRxiv*, doi:10.1101/2020.05.13.092619 (2020).

22 Brouwer, P. J. M. *et al.* Potent neutralizing antibodies from COVID-19 patients define multiple targets of vulnerability. *bioRxiv*, 2020.2005.2012.088716, doi:10.1101/2020.05.12.088716 (2020).

23 Chi, X. *et al.* A potent neutralizing human antibody reveals the N-terminal domain of the Spike protein of SARS-CoV-2 as a site of vulnerability. *bioRxiv*, 2020.2005.2008.083964, doi:10.1101/2020.05.08.083964 (2020).

24 Wang, C. *et al.* A human monoclonal antibody blocking SARS-CoV-2 infection. *Nat Commun* **11**, 2251, doi:10.1038/s41467-020-16256-y (2020).

25 Wang, P. *et al.* SARS-CoV-2 Neutralizing Antibody Responses Are More Robust in Patients with Severe Disease. *bioRxiv*, 2020.2006.2013.150250, doi:10.1101/2020.06.13.150250 (2020).

346 **Figure legends**

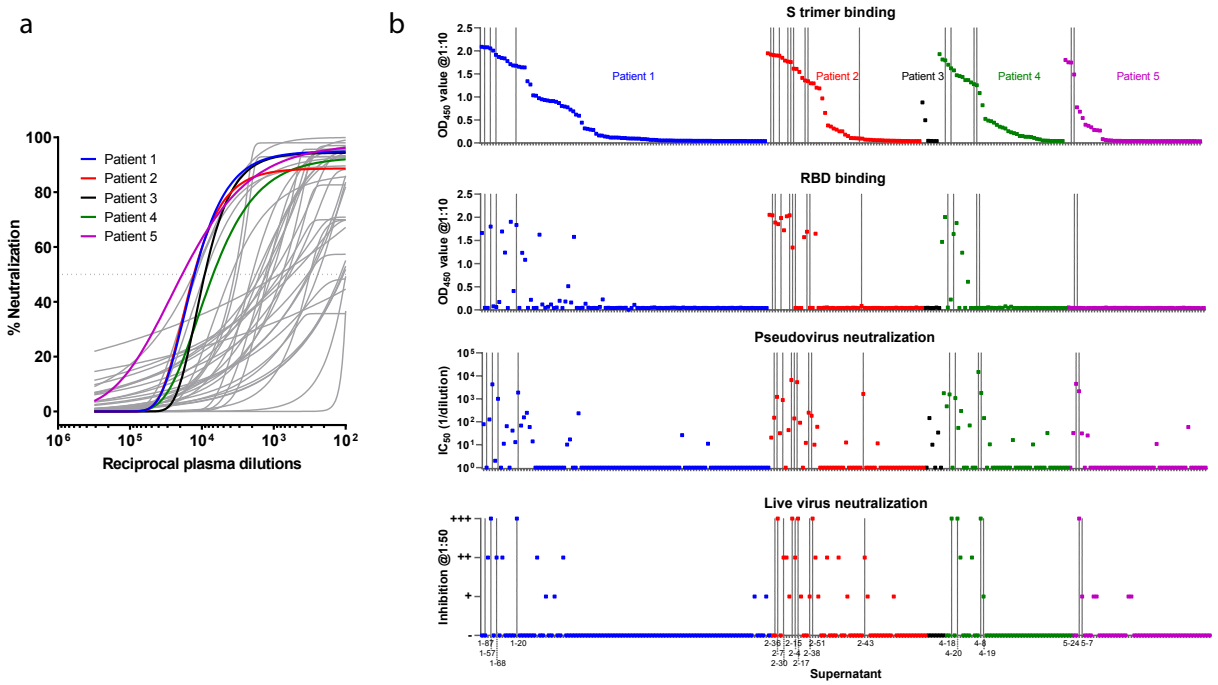

347 **Fig. 1 Isolation of SARS-CoV-2 mAbs from infected patients with severe disease. a**, Plasma
348 neutralization profile of 40 patients against SARS-CoV-2 pseudovirus (highlighted are 5 top
349 neutralizers chosen). **b**, All 252 transfection supernatants were screened for binding to S trimer
350 and RBD, as well as for neutralization against SARS-CoV-2 pseudovirus and live virus. For
351 pseudovirus neutralization, the 50% inhibitory dilutions (IC_{50}) of each supernatant were plotted.
352 For live virus, semi-quantitative representation of the inhibition at a dilution of 1:50, with
353 neutralization levels ranging from (-) for none to (+++) for complete neutralization, was plotted.
354 Potent antibodies later identified are marked by vertical lines and labelled at the bottom. The
355 antibodies from each patient are colored as in **a**.

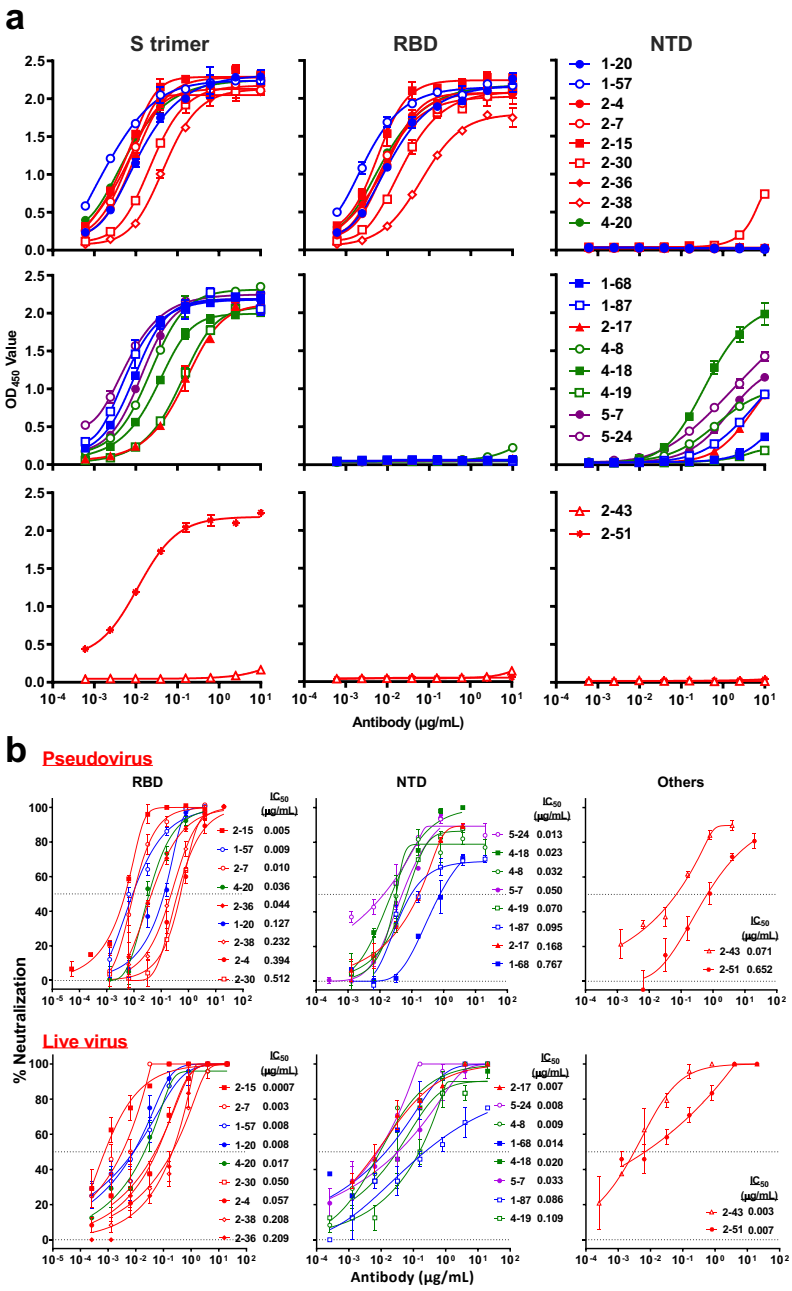

Fig. 2 Characterization of SARS-CoV-2 potent neutralizing mAbs. a, Binding profiles of 19 purified potent neutralizing mAbs against SARS-CoV-2 S trimer (left), RBD (middle), and NTD (right). Note that mAb 2-30 bound multiple proteins at high concentrations. **b**, The pseudovirus (top panels) and live virus (bottom panels) neutralization profiles for the 19 purified mAbs. Epitope classifications are listed on top of the panel b. Single replicate of the binding experiment and triplicates of neutralization are presented as mean ± SEM.

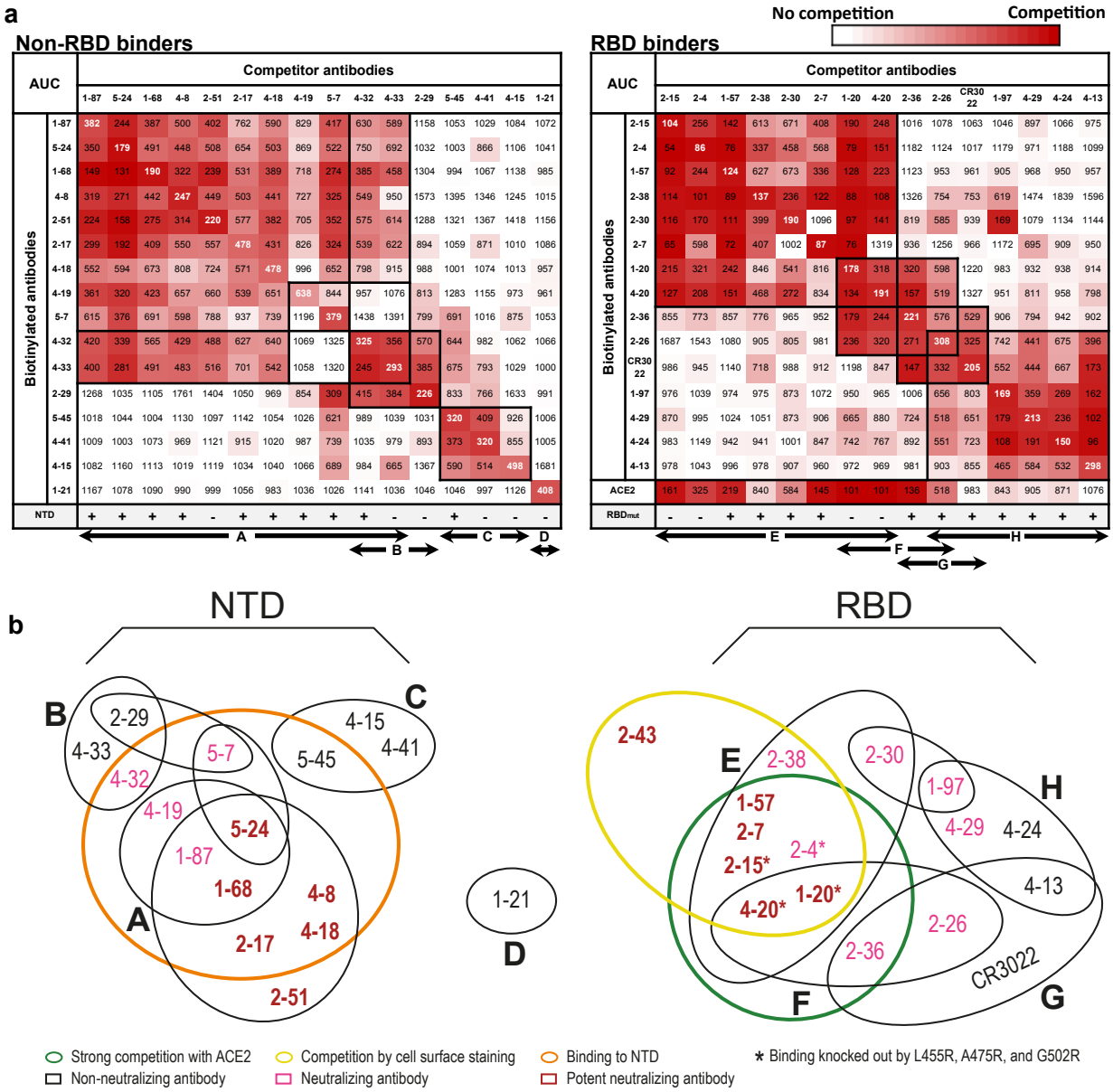

Fig. 3 Epitope mapping of select neutralizing and non-neutralizing mAbs. a, competition results of non-RBD binders (left) and RBD binders (right) in blocking ACE2 or biotinylated mAb binding to the S trimer. In addition, the ability to bind NTD and RBD_{mut} of each mAb is shown. The numbers in each box show the area under each competition curve (AUC) as tested by ELISA. +/- indicates binding/no binding of the mAb to the protein. The letters A to H at the bottom denote clusters of antibody epitopes defined by the competition experiments. **b**, Venn diagram interpretation of results from **a** and Extended Data Fig. 6b.

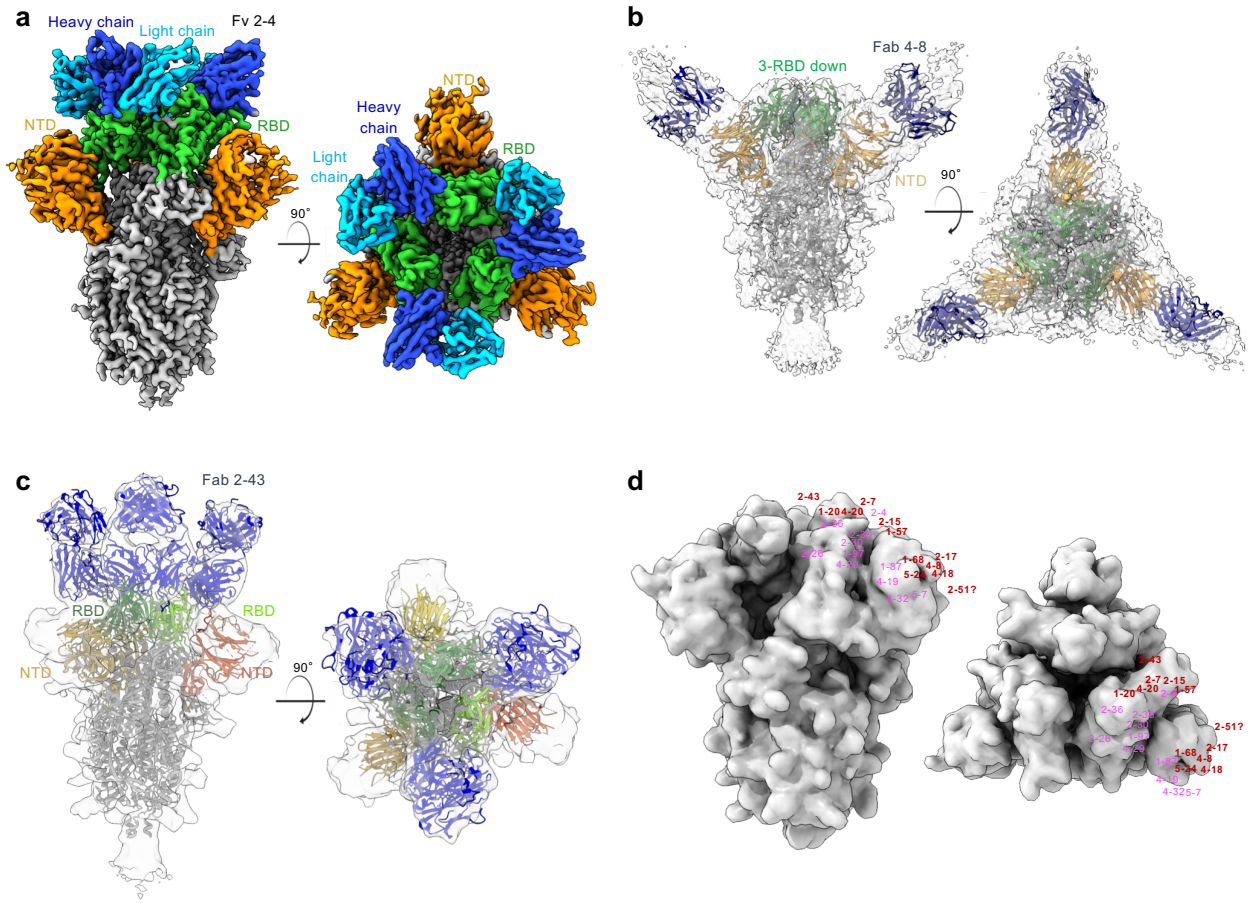

Figure 4. Cryo-EM reconstructions of Fab-spike complexes and visualization of neutralizing epitopes on the spike surface. a, Cryo-EM reconstruction of 2-4 Fab in complex with S trimer at 3.2 Å overall resolution. Density is colored with RBD in green, NTD in orange, and other regions in grey. **b,** Cryo-EM reconstruction of 4-8 Fab in complex with S trimer (ribbon diagram, colored as in a) at 3.9 Å overall resolution, with RBDs in the "all-down" configuration. **c,** Cryo-EM reconstruction of the 2-43 Fab in complex with S trimer at 5.8 Å resolution reveals a quaternary epitope involving RBD from one subunit and another RBD from the next. **d,** Mapping of the Venn diagrams from Fig. 3b onto the surface of the viral spike.

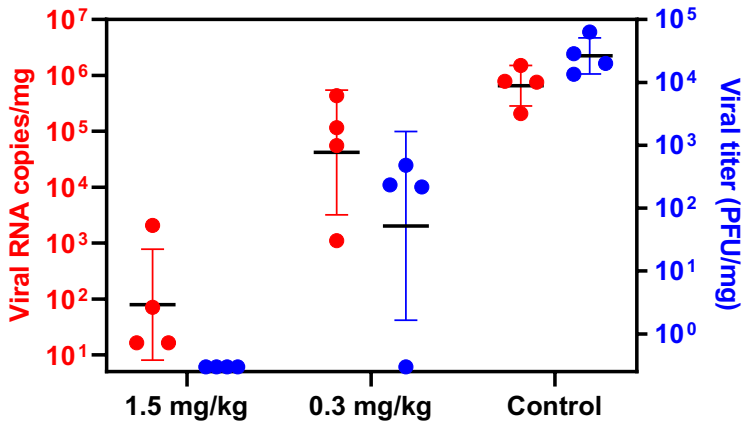

377 **Figure 5. Efficacy of mAb 2-15 in protecting against SARS-CoV-2 infection in lung tissues**
378 **of hamsters.** One day prior to intranasal challenge of SARS-CoV-2, each group of hamsters was
379 given a single intraperitoneal dose of 1.5 mg/kg of mAb 2-15 (n = 4), 0.3 mg/kg of mAb 2-15 (n
380 = 4), or saline as control (n = 4). The viral loads in the lung tissues on day 4 after viral challenge
381 were determined by qRT-PCR (red), as well as by an assay to quantify plaque forming units (PFU)
382 of infectious SARS-CoV-2 (blue). All data points are shown, along with the mean ± SD. The
383 differences between 1.5 mg/kg group and controls are statistically significant with p value <0.05.

384 **Methods**

385

386 **Expression and Purification of SARS-CoV-2 Proteins**

387 The mammalian expression vector that encodes the ectodomain of the SARS-CoV-2 S trimer and
388 the vector encoding RBD fused with SD1 at the N-terminus and an HRV-3C protease cleavage
389 site followed by a mFc tag and an 8xHis tag at the C-terminus were kindly provided by Jason
390 McLellan[4]. SARS-CoV-2 NTD (aa1-290) with an HRV-3C protease cleavage site, a mFc tag, and
391 an 8xHis tag at the C-terminus was also cloned into mammalian expression vector pCAGGS. Each
392 expression vector was transiently transfected into Expi293 cells using 1 mg/mL of
393 polyethylenimine (Polysciences). Five days post transfection, the S trimer was purified using
394 Strep-Tactin XT Resin (Zymo Research), and the RBD-mFc and NTD-mFc were purified using
395 protein A agarose (ThermoFisher Scientific). In order to obtain RBD-SD1 and NTD, the mFc and
396 8xHis tags at the C-terminus were removed by HRV-3C protease (Millipore-Sigma) and then
397 purified using Ni-NTA resin (Invitrogen) followed by protein A agarose.

398

399 **Sorting for S Trimer-Specific B cells and Single-Cell BCR Sequencing**

400 Peripheral blood mononuclear cells from five patients and one healthy donor were stained with
401 LIVE/DEAD™ Fixable Yellow Dead Cell Stain Kit (Invitrogen) at ambient temperature for 20
402 mins, followed by washing with RPMI-1640 complete medium and incubation with 10 µg/mL of
403 S trimer at 4˚C for 45 mins. Afterwards, the cells were washed again and incubated with a cocktail
404 of flow cytometry and hashtag antibodies, containing CD3 PE-CF594 (BD Biosciences), CD19
405 PE-Cy7 (Biolegend), CD20 APC-Cy7 (Biolegend), IgM V450 (BD Biosciences), CD27 PerCP-
406 Cy5.5 (BD Biosciences), anti-His PE (Biolegend), and human Hashtag 3 (Biolegend) at 4˚C for 1

407 hr. Stained cells were then washed, resuspended in RPMI-1640 complete medium and sorted for
408 S trimer-specific memory B cells (CD3-CD19+CD27+S trimer+ live single lymphocytes). The
409 sorted cells were mixed with mononuclear cells from the same donor, labeled with Hashtag 1, and
410 loaded into the 10X Chromium chip of the 5' Single Cell Immune Profiling Assay (10X Genomics)
411 at the Columbia University Human Immune Monitoring Core (HIMC; RRID:SCR_016740). The
412 library preparation and quality control were performed according to manufacturer's protocol and
413 sequenced on a NextSeq 500 sequencer (Illumina).
414
415 **Identification of S Trimer-Specific Antibody Transcripts**
416 For each sample, full-length antibody transcripts were assembled using the VDJ module in Cell
417 Ranger (version 3.1.0, 10X Genomics) with default parameters and the GRCh38 genome as
418 reference. To identify cells from the antigen sort, we first used the count module in Cell Ranger
419 to calculate copies of all hashtags in each cell from the Illumina NGS raw reads. High confidence
420 antigen-specific cells were identified as follows. Briefly, based on the copy numbers of the
421 hashtags observed, a cell must contain more than 100 copies of the antigen sort-specific hashtag
422 to qualify as an antigen-specific cell. Because hashtags can fall off from cells and bind to cells
423 from a different population in the sample mixture, each cell usually has both sorted and spiked-in-
424 specific hashtags. To enrich for true antigen-specific cells, the copy number of the specific hashtag
425 has to be at least 1.5x higher than that of the non-specific hashtag. Low quality cells were
426 identified and removed using the cell-calling algorithm in Cell Ranger. Cells that do not have
427 productive H and L chain pairs were excluded. If a cell contains more than two H or/and L chain
428 transcripts, the transcripts with less than 3 unique molecular identifiers were removed. Cells with
429 identical H and L chain sequences, which may have resulted from mRNA leakage, were merged

430 into one cell. Additional filters were applied to remove low quality cells and/or transcripts in the
431 antibody gene annotation process.
432
433 **Antibody Transcript Annotation and Selection Criteria**
434 Antigen-specific antibody transcripts were processed using our bioinformatics pipeline SONAR
435 for quality control and annotation[26]. Briefly, V(D)J genes were assigned for each transcript using
436 BLAST[27] with customized parameters against a germline gene database obtained from the
437 international ImMunoGeneTics information system (IMGT) database[26,28]. Based on BLAST
438 alignments of V and J regions, CDR3 was identified using the conserved second cysteine in the V
439 region and WGXG (H chain) or FGXG (L chain) motifs in the J region (X represents any amino
440 acid). For H chain transcripts, the constant domain 1 (CH1) sequences were used to assign isotype
441 using BLAST with default parameters against a database of human CH1 genes obtained from
442 IMGT. A BLAST E-value threshold of 1E-6 was used to find significant isotype assignments, and
443 the CH1 allele with the lowest E-value was used. Sequences other than the V(D)J region were
444 removed and transcripts containing incomplete V(D)J or/and frame shift were excluded. We then
445 aligned each of the remaining transcripts to the assigned germline V gene using CLUSTALO[29]
446 and calculated the somatic hypermutation level.
447
448 To select representative antibodies for functional characterization, we first clustered all antibodies
449 using USEARCH[30] with the following criteria: identical heavy chain V and J gene assignments,
450 the same length of CDRH3, and CDRH3 identity higher than 0.9. For each cluster, cells with the
451 same light chain V and J gene assignments were grouped into a clone. All clone assignments were
452 manually checked. We then calculated the clonal size for each clone, and one H and L chain pair

453 per clone was chosen for antibody synthesis. For clones with multiple members, the member with
454 the highest somatic hypermutation level was chosen for synthesis. For cells having multiple high
455 quality H or L chains, which may be from doublets, we synthesized all H and L chain combinations.
456

457 **Analysis of S Trimer-Specific Antibody Repertoire**

458 Because 88% of the S trimer-specific antibodies were IgG isotype, we therefore compared the
459 repertoire features to IgG repertoires from three healthy donors[31] (17,243 H chains, 27,575 kappa
460 L chains, 20,889 lambda L chains). The repertoire data from the three healthy donors were
461 combined and annotated using SONAR with the same process as above.
462

463 **Antibody Expression and Purification**

464 For each antibody, variable genes were optimized for human cell expression and synthesized by
465 GenScript. VH and VL were inserted separately into plasmids (gWiz or pcDNA3.4) that encode
466 the constant region for H chain and L chain. Monoclonal antibodies were expressed in Expi293
467 (ThermoFisher, A14527) by co-transfection of H chain and L chain expressing plasmids using
468 polyethylenimine and culture in 37°C shaker at 125 RPM and 8% CO_2. On day 3 post transfection,
469 400 μL of supernatant were collected for screening for binding to S trimer and RBD by ELISA,
470 and for neutralization of SARS-CoV-2 pseudovirus and authentic virus. Supernatants were also
471 collected on day 5 for antibody purification by rProtein A Sepharose (GE, 17-1279-01) affinity
472 chromatography.
473

474 **Production of Pseudoviruses**

475 Recombinant Indiana VSV (rVSV) expressing SARS-CoV-2 spike was generated as previously
476 described[32,33]. HEK293T cells were grown to 80% confluency before transfection with pCMV3-
477 SARS-CoV-2-spike (Sino Biological) using FuGENE 6 (Promega). Cells were cultured overnight
478 at 37°C with 5% CO_2. The next day, medium was removed and VSV-G pseudotyped ΔG-
479 luciferase (G*ΔG-luciferase, Kerafast) was used to infect the cells in DMEM at a MOI of 3 for
480 1 hr before washing the cells with 1X DPBS three times. DMEM supplemented with 2% fetal
481 bovine serum and 100 I.U./mL of penicillin and 100 μg/mL of streptomycin were added to the
482 inoculated cells, which were cultured overnight as described above. The supernatant was
483 harvested the following day and clarified by centrifugation at 300 g for 10 mins before aliquoting
484 and storing at −80°C.
485
486 **Pseudovirus Neutralization**
487 Neutralization assays were performed by incubating pseudoviruses with serial dilutions of heat-
488 inactivated plasma together with supernatant or purified antibodies, and scored by the reduction in
489 luciferase gene expression. In brief, Vero E6 cells (ATCC) were seeded in a 96-well plate at a
490 concentration of 2×10^4 cells per well. Pseudoviruses were incubated the next day with serial
491 dilutions of the test samples in duplicate or triplicate for 30 mins at 37°C. The mixture was added
492 to cultured cells and incubated for an additional 24 hrs. The luminescence was measured by
493 Britelite plus Reporter Gene Assay System (PerkinElmer). IC_{50} was defined as the dilution at
494 which the relative light units were reduced by 50% compared with the virus control wells (virus +
495 cells) after subtraction of the background in the control groups with cells only. The IC_{50} values
496 were calculated using non-linear regression in GraphPad Prism 8.0.
497

498 **Authentic SARS-CoV-2 Neutralization**

499 Supernatants containing expressed mAbs were diluted 1:10 and 1:50 in EMEM with 7.5%
500 inactivated fetal calf serum and incubated with authentic SARS-CoV-2 (strain USA-WA1/2020;
501 MOI 0.1) for 1hr at 37°C. Post-incubation, the mixture was transferred onto a monolayer of Vero-
502 E6 cells that was cultured overnight. After incubation of the cells with the mixture for 70 hrs at
503 37°C, cytopathic effects (CPE) caused by the infection were scored for each well from 0 to 4 to
504 indicate the degree of virus inhibition. Semi-quantitative representation of the inhibition for each
505 antibody-containing supernatant at a dilution of 1:50 is shown in the lowest panel of Fig. 1b with
506 neutralization levels ranging from (-) for none to (+++) for complete neutralization.

507

508 An end-point dilution assay in a 96-well plate format was performed to measure the neutralization
509 activity of select purified mAbs. In brief, each antibody was serially diluted (5-fold dilutions)
510 starting at 20 μg/mL. Triplicates of each mAb dilution were incubated with SARS-CoV-2 at a
511 MOI of 0.1 in EMEM with 7.5% inactivated fetal calf serum for 1 hr at 37ºC. Post incubation, the
512 virus-antibody mixture was transferred onto a monolayer of Vero-E6 cells grown overnight. The
513 cells were incubated with the mixture for 70 hrs. CPE were visually scored for each well in a
514 blinded fashion by two independent observers. The results were then converted into percentage
515 neutralization at a given mAb concentration, and the averages ± SEM were plotted using a five-
516 parameter dose-response curve in GraphPad Prism 8.0.

517

518 **Epitope Mapping by ELISA**

519 50 ng/well of S trimer, 50 ng/well of RBD, and 100 ng/well of NTD were coated on ELISA plates
520 at 4°C overnight. The ELISA plates were then blocked with 300 μL of blocking buffer (1% BSA

521 and 10% bovine calf serum (BCS) (Sigma) in PBS at 37°C for 2 hrs. Afterwards, supernatants
522 from the antibody transfection or purified antibodies were serially diluted using dilution buffer (1%
523 BSA and 20% BCS in PBS), incubated at 37°C for 1 hr. Next, 100 μL of 10,000-fold diluted
524 Peroxidase AffiniPure goat anti-human IgG (H+L) antibody (Jackson ImmunoResearch) were
525 added into each well and incubated for 1 hr at 37°C. The plates were washed between each step
526 with PBST (0.5% Tween-20 in PBS). Finally, the TMB substrate (Sigma) was added and
527 incubated before the reaction was stopped using 1M sulfuric acid. Absorbance was measured at
528 450 nm.
529
530 For the competition ELISA, purified mAbs were biotin-labeled using One-Step Antibody
531 Biotinylation Kit (Miltenyi Biotec) following manufacturer recommendations and purified using
532 40K MWCO Desalting Column (ThermoFisher Scientific). 50 μL of serially diluted competitor
533 antibodies were added into S trimer-precoated ELISA plates, followed by 50 μL of biotinylated
534 antibodies at a concentration that achieves an OD_{450} reading of 1.5 in the absence of competitor
535 antibodies. Plates were incubated at 37°C for 1 hr, and 100 μL of 500-fold diluted Avidin-HRP
536 (ThermoFisher Scientific) were added into each well and incubated for another 1 hr at 37°C. The
537 plates were washed by PBST between each of the previous steps. The plates were developed
538 afterwards with TMB and absorbance was read at 450 nm after the reaction was stopped.
539
540 For the ACE2 competition ELISA, 100 ng of ACE2 protein (Abcam) was immobilized on the
541 plates at 4°C overnight. The unbound ACE2 was washed away by PBST and then the plates were
542 blocked. After washing, 100 ng of S trimer in 50 μL of dilution buffer was added into each well,
543 followed by adding another 50 μL of serially diluted competitor antibodies and then incubating

544 the plates at 37°C for 1 hr. The ELISA plates were washed 4 times by PBST and then 100 μL of
545 2000-fold diluted anti-strep-HRP (Millipore Sigma) were added into each well for another 1 hr at
546 37°C. The plates were then washed, developed with TMB, and absorbance was read at 450 nm
547 after the reaction was stopped.
548
549 For all the competition ELISA experiments, the relative binding of biotinylated antibodies or
550 ACE2 to the S trimer in the presence of competitors was normalized by comparing to competitor-
551 free controls. Relative binding curve and the area under curve (AUC) were generated by fitting
552 the non-linear five-parameter dose-response curve in GraphPad Prism 8.0.
553
554 **Cell-Surface Competition Binding Assay**
555 Expi293 cells were co-transfected with vectors encoding pRRL-cPPT-PGK-GFP (Addgene) and
556 pCMV3-SARS-CoV-2 (2019-nCoV) Spike (Sino Biological) at a ratio of 1:1. Two days after
557 transfection, cells were incubated with a mixture of biotinylated mAb 2-43 (0.25 μg/mL) and
558 serially diluted competitor antibodies at 4°C for 1 hr. Then 100 μL of diluted APC-streptavidin
559 (Biolegend) were added to the cells and incubated at 4°C for 45 mins. Cells were washed 3 times
560 with FACS buffer before each step. Finally, cells were resuspended and 2-43 binding to cell-
561 surface S trimer was quantified on LSRII flow cytometer (BD Biosciences). The mean
562 fluorescence intensity of APC in GFP-positive cells was analyzed using FlowJo and the relative
563 binding of 2-43 to S trimer in the presence of competitors was calculated as the percentage of the
564 mean fluorescence intensity compared to that of the competitor-free controls.
565
566 **Cryo-EM Data Collection and Processing**

567 SARS-CoV-2 S trimer at a final concentration of 2 mg/ml was incubated with 6-fold molar excess
568 per spike monomer of the antibody Fab fragments for 30 minutes in 10 mM sodium acetate pH
569 5.5, 150 mM NaCl, and 0.005% n-Dodecyl-β-D-maltoside (DDM). 2 µL of sample were incubated
570 on C-flat 1.2/1.3 carbon grids for 30 secs and vitrified using a Leica EM GP Plunge Freezer. Data
571 were collected on a Titan Krios electron microscope operating at 300 kV equipped with a Gatan
572 K3 direct detector and energy filter using the Leginon software package[34]. A total electron fluence
573 of 51.3 e/Å^2 was fractionated over 40 frames, with a total exposure time of 2 secs. A magnification
574 of 81,000x resulted in a pixel size of 1.058 Å, and a defocus range of -0.4 to -3.5 µm was used.
575 All processing was done using cryoSPARC v2.14.2[35]. Raw movies were aligned and dose-
576 weighted using patch motion correction, and the CTF was estimated using patch CTF estimation.
577 A small subset of approximately 200 micrographs were picked using blob picker, followed by 2D
578 classification and manual curation of particle picks, and used to train a Topaz neural network[36].
579 This network was then used to pick particles from the remaining micrographs, which were
580 extracted with a box size of 384 pixels.
581
582 For the 2-4 Fab dataset, 2D classification followed by *ab initio* modelling and 3D heterogeneous
583 refinement revealed 83,927 particles with three 2-4 Fabs bound, one to each RBD. A
584 reconstruction of these particles using Non-Uniform Refinement with imposed C3 symmetry
585 resulted in a 3.6 Å map, as determined by the gold standard FSC. Given the relatively low
586 resolution of the RBD-Fab interface, masked local refinement was used to obtain a 3.5 Å map with
587 significantly improved density. A masked local refinement of the remainder of the S timer resulted
588 in a 3.5 Å reconstruction. These two local refinements were aligned and combined using the vop
589 maximum function in UCSF Chimera[37]. This was repeated for the half maps, which were used,

590 along with the refinement mask from the global Non-Uniform refinement, to calculate the
591 3DFSC[38] and obtain an estimated resolution of 3.2 Å. All maps have been submitted to the EMDB
592 with the ID EMD-22156.
593
594 For the 4-8 Fab dataset, image preprocessing and particle picking was performed as above. 2D
595 classification, *ab initio* modelling, and 3D heterogeneous classification revealed 47,555 particles
596 with 3 Fabs bound, one to each NTD and with all 3 RBDs in the down conformation. While this
597 particle stack was refined to 3.9 Å using Non-Uniform refinement with imposed C3 symmetry,
598 significant molecular motion prevented the visualization of the Fab epitope at high resolution
599 (EMD-22159). In addition, 105,278 particles were shown to have 3 Fabs bound, but with 1 RBD
600 in the up conformation. These particles were refined to 4.0 Å using Non-Uniform refinement with
601 C1 symmetry (EMD-22158), and suffered from the same conformational flexibility as the all-
602 RBD-down particles. This flexibility was visualized using 3D variability analysis in cryoSPARC.
603
604 For the 2-43 Fab dataset, which was collected at an electron fluence of 51.69 e/Å2, image
605 preprocessing was performed as above, and particle picking was performed with blob picker. 2D
606 classification, *ab initio* modelling, and 3D heterogeneous classification revealed 10,068 particles
607 with 3 Fabs bound, which was refined to 5.8Å resolution (EMD-22157).
608
609 **Cryo-EM Model Fitting**
610 An initial homology model of the 2-4 Fab was built using Schrodinger Release 2020-2:
611 BioLuminate[39]. The RBD was initially modeled using the coordinates from PDB ID 6W41. The
612 remainder of the S timer was modeled using the coordinates from PDB ID 6VSB. These models

613 were docked into the consensus map using Chimera. The model was then fitted interactively using
614 ISOLDE 1.0b5[40] and COOT 0.8.9.2[41], and using real space refinement in Phenix 1.18[42]. In cases
615 where side chains were not visible in the experimental data, they were truncated to alanine.
616 Validation was performed using Molprobity[43] and EMRinger[44]. The model was submitted to the
617 PDB with the ID 6XEY. Figures were prepared using ChimeraX[45].
618
619 **Hamster Protection Experiment**
620 *In vivo* evaluation of mAb 2-15 in an established golden Syrian hamster model of SARS-CoV-2
621 infection was performed as described previously with slight modifications[46]. Approval was
622 obtained from the University of Hong Kong (HKU) Committee on the Use of Live Animals in
623 Teaching and Research. Briefly, 6-8-week-old male and female hamsters were obtained from the
624 Chinese University of Hong Kong Laboratory Animal Service Centre through the HKU
625 Laboratory Animal Unit and kept in Biosafety Level-2 (BSL-2) housing with access to standard
626 pellet feed and water *ad libitum* until virus challenge in the BSL-3 animal facility. Each hamster
627 (n = 4 per group) was intraperitoneally administered one dose of 1.5 mg/kg of mAb 2-15 in
628 phosphate-buffered saline (PBS), 0.3 mg/kg of mAb 2-15 in PBS, or PBS alone as control.
629 Twenty-four hours later, each hamster was intranasally inoculated with a challenge dose of 100
630 μL of Dulbecco's Modified Eagle Medium containing 10^5 PFU of SARS-CoV-2 (HKU-001a strain,
631 GenBank accession no: MT230904.1) under intraperitoneal ketamine (200 mg/kg) and xylazine
632 (10 mg/kg) anesthesia. The hamsters were monitored twice daily for clinical signs of disease and
633 sacrificed at day 4 post-challenge. Half of each hamster's lung tissues were used for viral load
634 determination by a quantitative SARS-CoV-2 RdRp/Hel reverse transcription-polymerase chain
635 reaction assay[47] and an infectious virus titration using a plaque assay described previously[46].

636 Student's *t* test was used to determine significant differences among the groups, and a p value of
637 < 0.05 was considered statistically significant.
638
639 **Data Availability**
640 The 19 neutralizing antibodies were deposited to Genbank with accession numbers from
641 MT712278 to MT712315. Coordinates for the antibody 2-4 complex are deposited in the Protein
642 Data Bank as PDB 6XEY. Cryo-EM maps and data are deposited in EMDB with deposition codes
643 EMDB-22156 for antibody 2-4, EMDB-22158 and EMDB-22159 for antibody 4-8, and EMDB-
644 22275 for antibody 2-43. These data are used in Fig. 4 and Extended Data Figs. 7, 8, 9, 10, and 11.
645
646 **Code Availability**
647 Next-generation sequencing data of antibody repertoires were processed using Cell ranger v3.1.0,
648 SONAR V1, BLAST v2.2.25, CLUSTALO1.2.3, and USEARCH v9.2.64. Cryo-EM data was
649 collected using Leginon 3.4.beta. Cryo-EM data was processed using cryoSPARC v2.14.2,
650 MotionCor2, Topaz v0.2.4, 3DFSC v3.0, UCSF Chimera v1.13.1, ChimeraX v0.93, ISOLDE
651 v1.0b5, Phenix v1.18, and COOT v0.8.9.2.

652 **Methods references**

653 26 Schramm, C. A. *et al.* SONAR: A High-Throughput Pipeline for Inferring Antibody
654 Ontogenies from Longitudinal Sequencing of B Cell Transcripts. *Frontiers in immunology*
655 **7**, 372, doi:10.3389/fimmu.2016.00372 (2016).
656 27 Altschul, S. F. *et al.* Gapped BLAST and PSI-BLAST: a new generation of protein database
657 search programs. *Nucleic Acids Res* **25**, 3389-3402 (1997).
658 28 Lefranc, M. P. *et al.* IMGT, the international ImMunoGeneTics information system. *Nucleic*
659 *Acids Res* **37**, D1006-1012, doi:10.1093/nar/gkn838 (2009).
660 29 Sievers, F. & Higgins, D. G. Clustal Omega, Accurate Alignment of Very Large Numbers of
661 Sequences. *Multiple Sequence Alignment Methods* **1079**, 105-116, doi:10.1007/978-1-
662 62703-646-7_6 (2014).
663 30 Edgar, R. C. Search and clustering orders of magnitude faster than BLAST. *Bioinformatics*
664 **26**, 2460-2461, doi:10.1093/bioinformatics/btq461 (2010).
665 31 Sheng, Z. *et al.* Gene-Specific Substitution Profiles Describe the Types and Frequencies of
666 Amino Acid Changes during Antibody Somatic Hypermutation. *Frontiers in immunology* **8**,
667 537 (2017).
668 32 Nie, J. *et al.* Establishment and validation of a pseudovirus neutralization assay for SARS-
669 CoV-2. *Emerg Microbes Infect* **9**, 680-686, doi:10.1080/22221751.2020.1743767 (2020).
670 33 Whitt, M. A. Generation of VSV pseudotypes using recombinant DeltaG-VSV for studies
671 on virus entry, identification of entry inhibitors, and immune responses to vaccines. *J Virol*
672 *Methods* **169**, 365-374, doi:10.1016/j.jviromet.2010.08.006 (2010).
673 34 Suloway, C. *et al.* Automated molecular microscopy: the new Leginon system. *J Struct Biol*
674 **151**, 41-60, doi:10.1016/j.jsb.2005.03.010 (2005).
675 35 Punjani, A., Rubinstein, J. L., Fleet, D. J. & Brubaker, M. A. cryoSPARC: algorithms for rapid
676 unsupervised cryo-EM structure determination. *Nat Methods* **14**, 290-296,
677 doi:10.1038/nmeth.4169 (2017).
678 36 Bepler, T. *et al.* Positive-unlabeled convolutional neural networks for particle picking in
679 cryo-electron micrographs. *Nature Methods* **16**, 1153-1160, doi:10.1038/s41592-019-
680 0575-8 (2019).
681 37 Pettersen, E. F. *et al.* UCSF Chimera--a visualization system for exploratory research and
682 analysis. *J Comput Chem* **25**, 1605-1612, doi:10.1002/jcc.20084 (2004).
683 38 Tan, Y. Z. *et al.* Addressing preferred specimen orientation in single-particle cryo-EM
684 through tilting. *Nat Methods* **14**, 793-796, doi:10.1038/nmeth.4347 (2017).
685 39 Zhu, K. *et al.* Antibody structure determination using a combination of homology
686 modeling, energy-based refinement, and loop prediction. *Proteins* **82**, 1646-1655,
687 doi:10.1002/prot.24551 (2014).
688 40 Croll, T. I. ISOLDE: a physically realistic environment for model building into low-resolution
689 electron-density maps. *Acta Crystallogr D Struct Biol* **74**, 519-530,
690 doi:10.1107/S2059798318002425 (2018).
691 41 Emsley, P. & Cowtan, K. Coot: model-building tools for molecular graphics. *Acta*
692 *Crystallogr D Biol Crystallogr* **60**, 2126-2132, doi:10.1107/S0907444904019158 (2004).

42 Adams, P. D. *et al.* Recent developments in the PHENIX software for automated crystallographic structure determination. *J Synchrotron Radiat* **11**, 53-55, doi:10.1107/s0909049503024130 (2004).

43 Davis, I. W., Murray, L. W., Richardson, J. S. & Richardson, D. C. MOLPROBITY: structure validation and all-atom contact analysis for nucleic acids and their complexes. *Nucleic Acids Res* **32**, W615-619, doi:10.1093/nar/gkh398 (2004).

44 Barad, B. A. *et al.* EMRinger: side chain-directed model and map validation for 3D cryo-electron microscopy. *Nat Methods* **12**, 943-946, doi:10.1038/nmeth.3541 (2015).

45 Goddard, T. D. *et al.* UCSF ChimeraX: Meeting modern challenges in visualization and analysis. *Protein Sci* **27**, 14-25, doi:10.1002/pro.3235 (2018).

46 Chan, J. F. *et al.* Simulation of the clinical and pathological manifestations of Coronavirus Disease 2019 (COVID-19) in golden Syrian hamster model: implications for disease pathogenesis and transmissibility. *Clin Infect Dis*, doi:10.1093/cid/ciaa325 (2020).

47 Chan, J. F. *et al.* Improved Molecular Diagnosis of COVID-19 by the Novel, Highly Sensitive and Specific COVID-19-RdRp/Hel Real-Time Reverse Transcription-PCR Assay Validated In Vitro and with Clinical Specimens. *J Clin Microbiol* **58**, doi:10.1128/JCM.00310-20 (2020).

710 **Acknowledgements**

711 We thank N. Wang and J. McLellan for providing reagents for generating the SARS-CoV-2 S
712 trimer and RBD-SD1 with mFc tag. We thank W. Chen for assistance with generating the Venn
713 diagrams, and B. DeKosky and X. Wu for helpful input. This study was supported by funding to
714 D.D.H. from the Jack Ma Foundation, the JPB Foundation, Samuel Yin, Brii Biosciences, Tencent
715 Charity Foundation, Roger Wu, Carol Ludwig, and Peggy and Andrew Cherng. Cryo-EM data
716 collection was performed at the National Center for CryoEM Access and Training and the Simons
717 Electron Microscopy Center located at the New York Structural Biology Center, supported by the
718 NIH Common Fund Transformative High Resolution Cryo-Electron Microscopy program (U24
719 GM129539) and by grants from the Simons Foundation (SF349247) and NY State Assembly. Data
720 analysis was performed at the National Resource for Automated Molecular Microscopy
721 (NRAMM), supported by the NIH National Institute of General Medical Sciences (GM103310).
722 Hamster experiments were conducted with support from the Health@InnoHK (Centre for Virology,
723 Vaccinology and Therapeutics), Innovation and Technology Commission, The Government of the
724 Hong Kong Special Administrative Region.

725

726 **Author Contributions**

727 D.D.H conceived of the project. L.L., P.W., M.S.N, J.Y., Q.W., Y.H. performed many of the
728 experiments. M.T.Y. was responsible for recruiting patients, obtaining clinical specimens, and
729 summarizing clinical data. L.L., V.S., A.F. and X.V.G. performed and analyzed the B-cell sorting,
730 10X Genomics, sequencing and analysis of the clones. Z.S. performed bioinformatic analyses on
731 10X next-generation sequencing data and antibody repertoire. J.Y. cloned, expressed, and purified
732 the mAbs. L.L. and Q.W. performed the epitope mapping and binding experiments. P.W.

733 conducted the pseudovirus neutralization assays and M.S.N. and Y.X. performed infectious SARS-
734 CoV-2 neutralization assays. M.A.R., G.C., J.B, J.G., and L.S. carried out the cryo-EM studies.
735 J.F-W.C., Z.C., and K-Y.Y. were responsible for the hamster experiment. Y.L. helped with project
736 management. T.Z. and P.D.K. provided key reagents for the study, and P.D.K. contributed to the
737 analysis and discussion of the data. L.L., P.W., M.S.N., J.Y., Y.H., Z.S., M.A.R., Q.W, L.S., and
738 D.D.H analyzed the results, and D.D.H. wrote the manuscript, with contributions from each author.
739 J.G.S. provided valuable suggestions.
740

741 **Ethic Statement**

742 Acquiring convalescent specimens to isolate and identify potent monoclonal antibodies against
743 COVID-19" (AAAS9517) was approved by the Columbia University Institutional Review Board.
744 Informed consent was obtained from all participants or surrogates.
745

746 **Competing Interest Declaration**

747 A provisional patent application has been filed for the monoclonal antibodies described in the
748 manuscript. L.L. and D.D.H. are inventors.

749 **Extended Data**

750

751 **Extended Data Table 1 Patient information**

Patient	Age	Sex & Race	Days from symptom onset to:	Biomarker	Complications	Outcome
1	57	Female, Hispanic	Admission: 7 MV: 12 Ab isolation: 18	hsCRP = 208 mg/L ESR = 58 mm/hr IL-6 = 23 pg/mL Ferritin = 766 ng/mL D-dimer = 3.4 μg/mL FEU	ARDS	Discharged on day 30
2	71	Female, Hispanic	Admission: 20 MV: 20 Ab isolation: 29	hsCRP = 33 mg/L ESR > 130 mm/hr IL-6 = 13 pg/mL Ferritin = 425 ng/mL D-dimer = 5.7 μg/mL FEU	ARDS Ventilator associated pneumonia	Discharged on day 45
3	61	Male, White	Admission: 10 MV: 10 Ab isolation: 21	hsCRP = 51 mg/L ESR = 57 mm/hr IL-6 > 315 pg/mL Ferritin = 3,238 ng/mL D-dimer = 7.4 μg/mL FEU	ARDS Acute kidney injury (hemodialysis) Sepsis	Death on day 28
4	51	Male, Black	Admission: 7 MV: 10 Ab isolation: 25	hsCRP = 88 mg/L ESR = 110 mm/hr IL-6 = 77 pg/mL Ferritin = 510 ng/mL D-dimer = 13.4 μg/mL FEU	ARDS Acute kidney injury (no hemodialysis) Ventilator associated pneumonia	Discharged on day 51
5	50	Male, White	Admission: 5 MV: 7 Ab isolation: 32	hsCRP = 2 mg/L ESR = 63 mm/hr	ARDS Neuropathy	Discharged on day 27

752 Abbreviation: ARDS, acute respiratory distress syndrome; MV, mechanical ventilation; hsCRP,
753 high sensitivity C-reactive protein, ULN>10 mg/L; ESR, erythrocyte sedimentation rate,
754 ULN=20 mm/hr; Interleukin 6, ULN= 5 pg/mL; Ferritin, ULN=150 ng/mL; D-dimer quantitative
755 ULN= 0.8ug/mL FEU.

756 **Extended Data Table 2 Cryo-EM data collection, refinement, and validation statistics**.

	SARS-CoV-2 spike with Fab 2-4 (EMDB-22156) (PDB 6XEY)	SARS-CoV-2 spike RBD up with Fab 4-8 (EMDB-22158)	SARS-CoV-2 spike RBD down with Fab 4-8 (EMDB-22159)	SARS-CoV-2 spike with Fab 2-43 (EMDB-22275)
Data collection and processing				
Magnification	81,000	81,000	81,000	81,000
Voltage (kV)	300	300	300	300
Electron exposure (e–/Å^2)	51.30	51.30	51.30	51.69
Defocus range (μm)	-0.4 to -3.5	-0.4 to -3.5	-0.4 to -3.5	-0.4 to -3.5
Pixel size (Å)	1.058	1.058	1.058	1.058
Symmetry imposed	C3	C1	C3	C1
Initial particle images (no.)	556,983	256,848	256,848	55,161
Final particle images (no.)	83,927	105,278	47,555	10,068
Map resolution (Å)	3.25	4.0	3.9	5.8
FSC threshold	0.143	0.143	0.143	0.143
Map resolution range (Å)	406.3-3.25	406.3-4.0	406.3-3.9	406.3-5.8
Refinement				
Initial model used (PDB code)	6VSB			
Model resolution (Å)	3.7			
FSC threshold	0.5			
Model resolution range (Å)	406.3-3.25			
Map sharpening *B* factor (Å^2)	-97.5			
Model composition				
Non-hydrogen atoms	28,482			
Protein residues	3788			
Ligands	63			
B factors (Å^2)				
Protein	54.35			
Ligand	73.91			
R.m.s. deviations				
Bond lengths (Å)	0.005			
Bond angles (°)	0.810			
Validation				
MolProbity score	1.51			
Clashscore	3.59			
Poor rotamers (%)	0.22			
Ramachandran plot				
Favored (%)	94.75			
Allowed (%)	5.17			
Disallowed (%)	0.08			

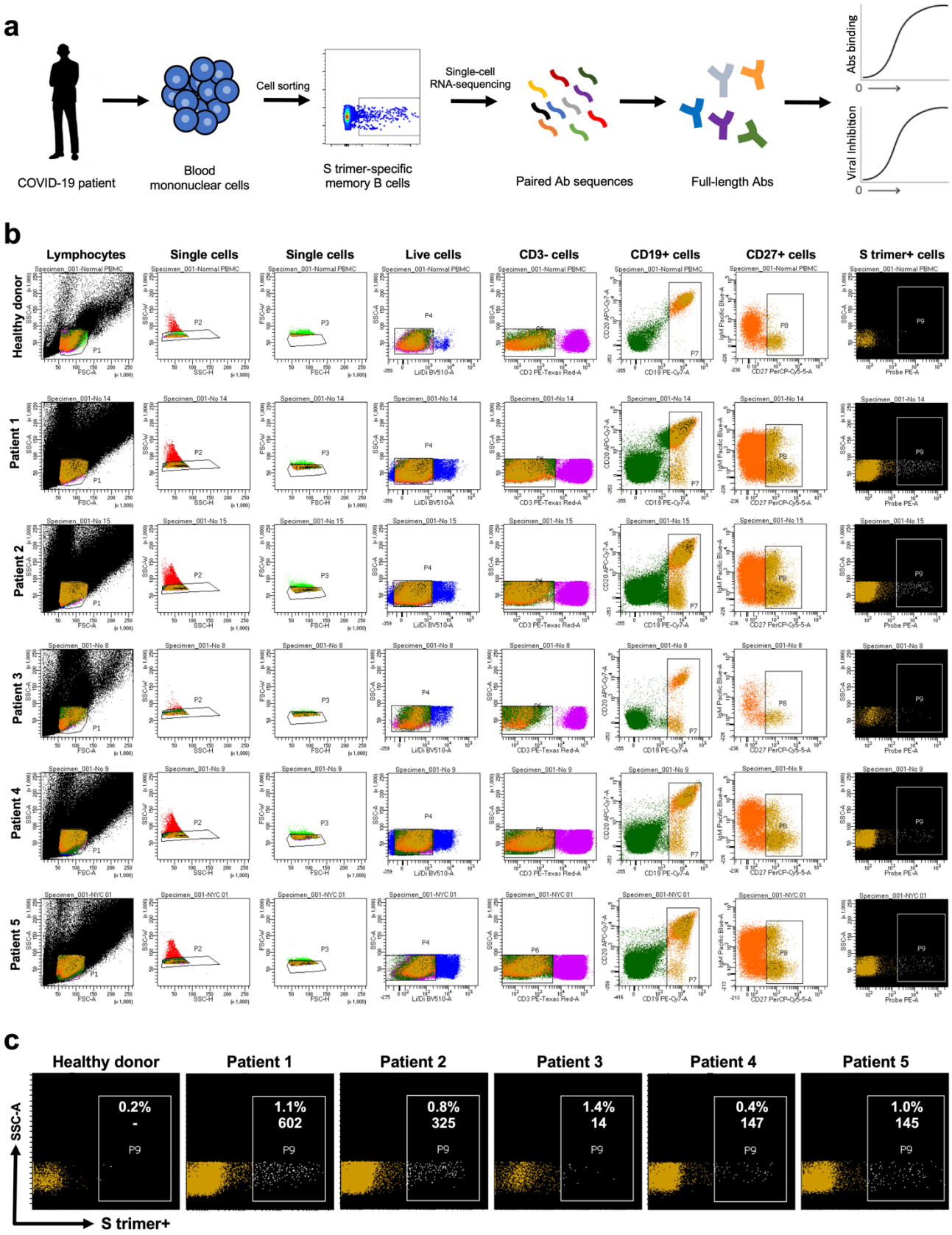
a
COVID-19 patient
Blood mononuclear cells
Cell sorting
S trimer-specific memory B cells
Single-cell RNA-sequencing
Paired Ab sequences
Full-length Abs
Abs binding
Viral Inhibition
b
Lymphocytes
Single cells
Single cells
Live cells
CD3- cells
CD19+ cells
CD27+ cells
S trimer+ cells
Healthy donor
Patient 1
Patient 2
Patient 3
Patient 4
Patient 5
c
Healthy donor
Patient 1
Patient 2
Patient 3
Patient 4
Patient 5
0.2%
-
1.1%
602
0.8%
325
1.4%
14
0.4%
147
1.0%
145
P9
SSC-A
S trimer+

758 **Extended Data Fig. 1 SARS-CoV-2 S trimer-specific antibody isolation strategy. a**, Schema
759 for isolating of S trimer-specific mAbs from memory B cells in the blood of infected patients. **b**,
760 Sorting results on the isolation of S trimer-specific memory B cells using flow cytometry. **c**,
761 Magnified representation of the panel of S trimer-positive memory B cells for each patient. Inset
762 numbers indicate the absolute number and the percentage of S trimer-specific memory B cells
763 isolated from each case.

a

	Abs tested	Binding Abs			Neutralizing Abs	Neutralizing Abs
		S trimer	RBD	Non-RBD	Pseudovirus	Live virus
Total	252	121	38	83	61	41
Patient 1	100	45	19	26	19	11
Patient 2	54	29	12	17	18	18
Patient 3	6	2	0	2	3	0
Patient 4	44	32	7	25	14	6
Patient 5	48	13	0	13	7	6

b

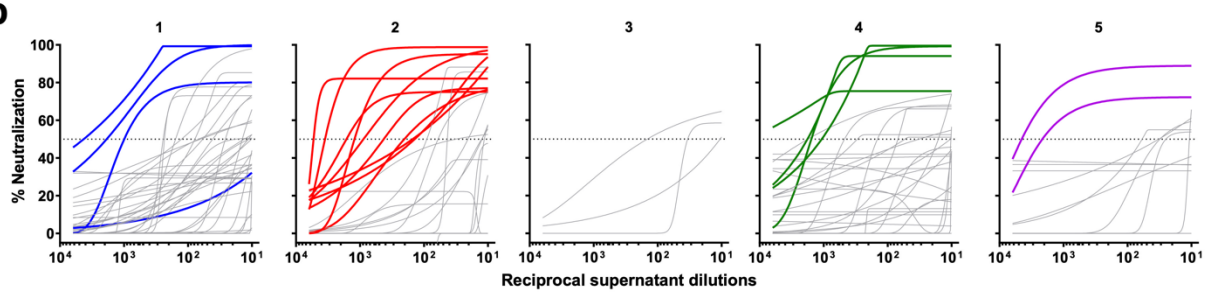

764 **Extended Data Fig. 2 Summary of mAb screening of transfection supernatants. a,** Numbers
765 of binding and neutralizing antibodies from patients 1 to 5. **b,** The best-fit pseudovirus
766 neutralization curves for 130 samples that were positive in at least one of the screens shown in Fig.
767 1b. The 18 transfection supernatants that showed evidently better potency are highlighted in colors,
768 while others with non-neutralizing or weakly neutralizing activities are shown in grey. One
769 additional supernatant (Patient 1) that was initially missed in the pseudovirus screen but later found
770 to be a potent neutralizing mAb (1-87) is also highlighted.

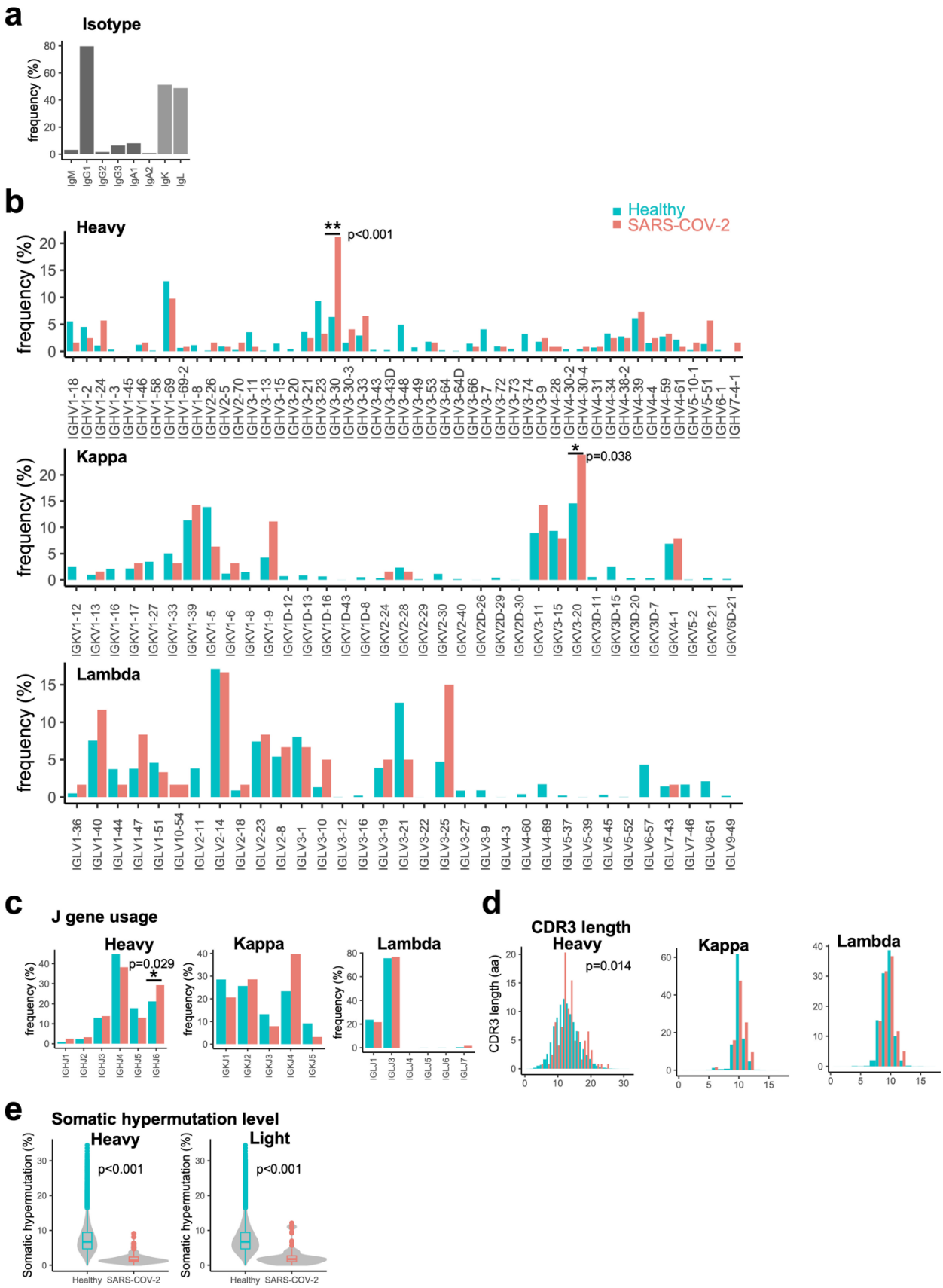
a
Isotype
frequency (%)
IgM
IgG1
IgG2
IgG3
IgA1
IgA2
IgK
IgL
b
Healthy
SARS-COV-2
Heavy
** p<0.001
Kappa
* p=0.038
Lambda
c
J gene usage
Heavy
p=0.029
Kappa
Lambda
d
CDR3 length
Heavy
p=0.014
Kappa
Lambda
CDR3 length (aa)
e
Somatic hypermutation level
Heavy
p<0.001
Light
p<0.001
Somatic hypermutation (%)
Healthy
SARS-COV-2

772 **Extended Data Fig. 3 Genetic features of SARS-CoV-2-specific antibody repertoire. a,** 108
773 of the 123 antigen-specific antibodies are from IgG isotype. The kappa and lambda light chains
774 are comparably used. **b,** Compared to IgG repertoires of healthy human donors (17,243, 27,575,
775 and 20,889 transcripts for heavy, kappa, and lambda chains respectively), IGHV3-30 (antigen-
776 specific n=26 and healthy donor n=1117) and IGKV3-20 genes (antigen-specific n=15 and healthy
777 donor n=4,071) are over-represented in heavy and light chain repertoires respectively (P values
778 are 6.415e-11 and 0.04332 respectively, $\chi 2$-test with 1 degree of freedom). We did not test the
779 enrichment of other genes because the numbers of antigen-specific antibodies are less than 15. **c,**
780 The usage of IGHJ6 gene (antigen-specific n=36 and healthy donor n=3646) was significantly
781 higher in antigen-specific antibodies ($\chi 2$-test with 1 degree of freedom, p=0.02807). **d,** The
782 CDRH3 length of antigen-specific antibodies is significantly longer than in healthy donors (two-
783 sided Kolmogorov–Smirnov test, p=0.014). **e,** For both heavy and light chains, the V region
784 nucleotide somatic hypermutation levels are significantly lower than in antibodies of healthy
785 donors (two-sided Kolmogorov–Smirnov test, p< 2.2e-16 for both heavy and light chains). For the
786 boxplots, the middle lines are medians. The lower and upper hinges correspond to the first and
787 third quartiles respectively. The upper whisker extends to values no larger than 1.5*IQR (the inter-
788 quartile range or distance between the first and third quartiles) from the hinge. The lower whisker
789 extends to values no smaller than 1.5 * IQR from the hinge. Data points beyond the whiskers were
790 plotted as outliers using dots.
791

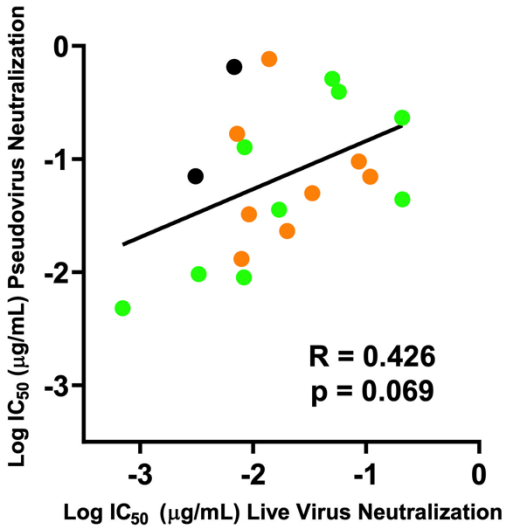

792 **Extended Data Fig. 4 Correlation of neutralizing antibody titers of the top 19 mAbs in the**
793 **live SARS-CoV-2 assay versus the pseudovirus assay.** Green circles represent RBD-directed
794 antibodies; orange circles represent NTD-directed antibodies; and black circles represent
795 antibodies in the "Others" category. The *Pearson correlation coefficient (r)* and the *p* value were
796 calculated using GraphPad Prism. Experiments were performed in triplicates for all mAbs tested.

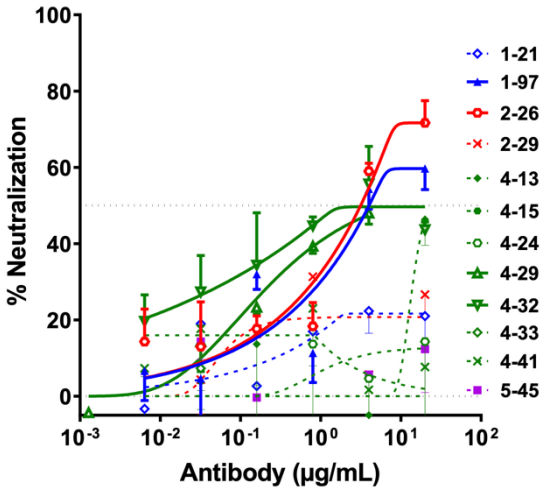

797 **Extended Data Fig. 5 The pseudovirus neutralization profiles for 12 purified mAbs that**
798 **strongly bound the S trimer but with weak or no virus-neutralizing activities.** The four mAbs
799 with weak neutralizing activities against SARS-CoV-2 pseudovirus are shown in sold lines, and
800 the remaining 8 non-neutralizing mAbs are shown in dashed lines.

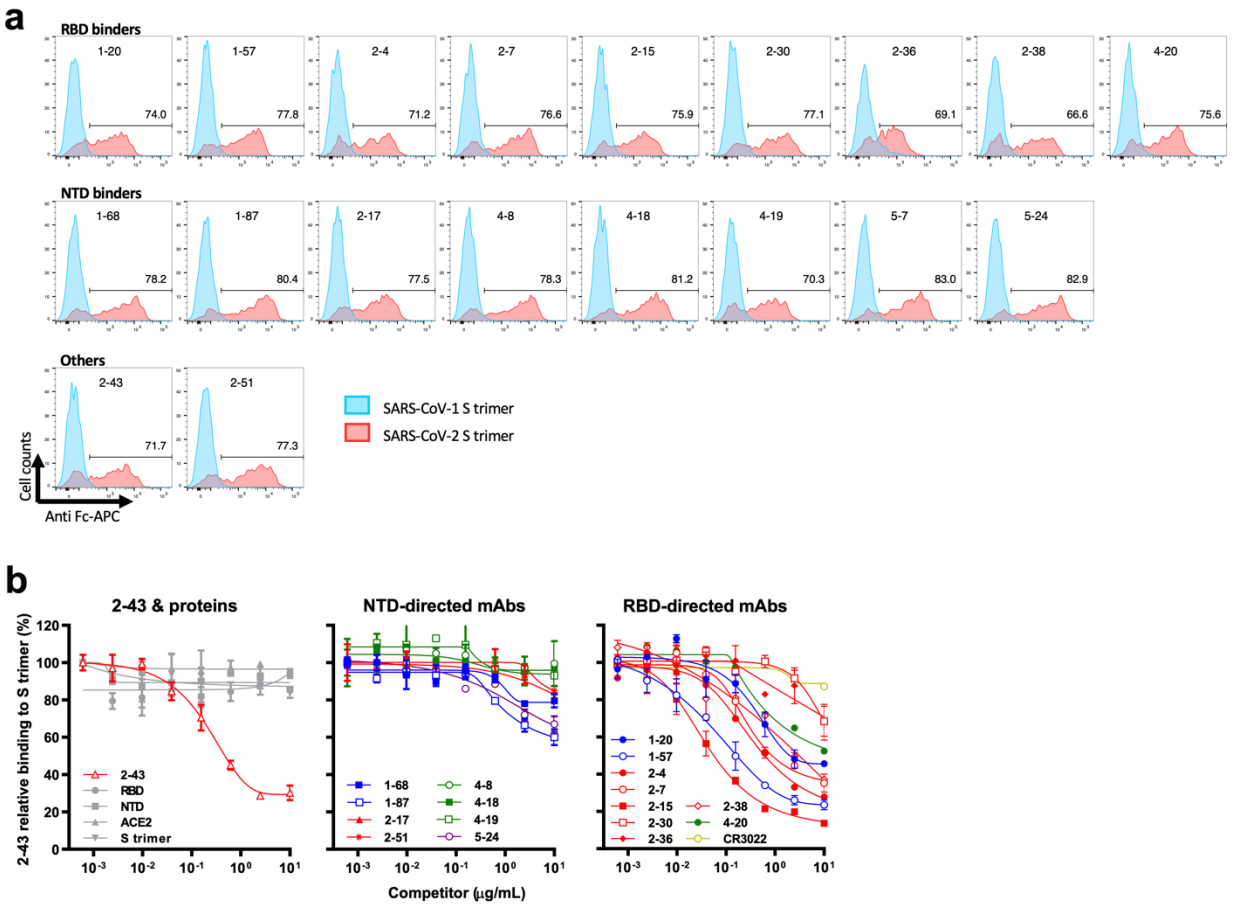

Extended Data Fig. 6 Cell-surface staining with antibodies a, Antibody binding to the SARS-CoV-1 (blue) and SARS-CoV-2 (red) spike proteins expressed on the cell surface. Expi293 cells were co-transfected with GFP and full-length SARS-CoV-1 or SARS-CoV-2 spike genes. After 48 hours, antibody binding to spike protein in the GFP-positive cells was detected by flow cytometer. The data show all antibodies tested were able to recognize the wildtype SARS-CoV-2 spike protein but not SARS-CoV-1 spike protein. **b,** Monoclonal Ab 2-43 bound to S trimer expressed on Expi293 cell surface can be competed out by mAbs directed to RBD but only minimally by mAbs to the NTD region. Shown are representative data from three independent experiments.

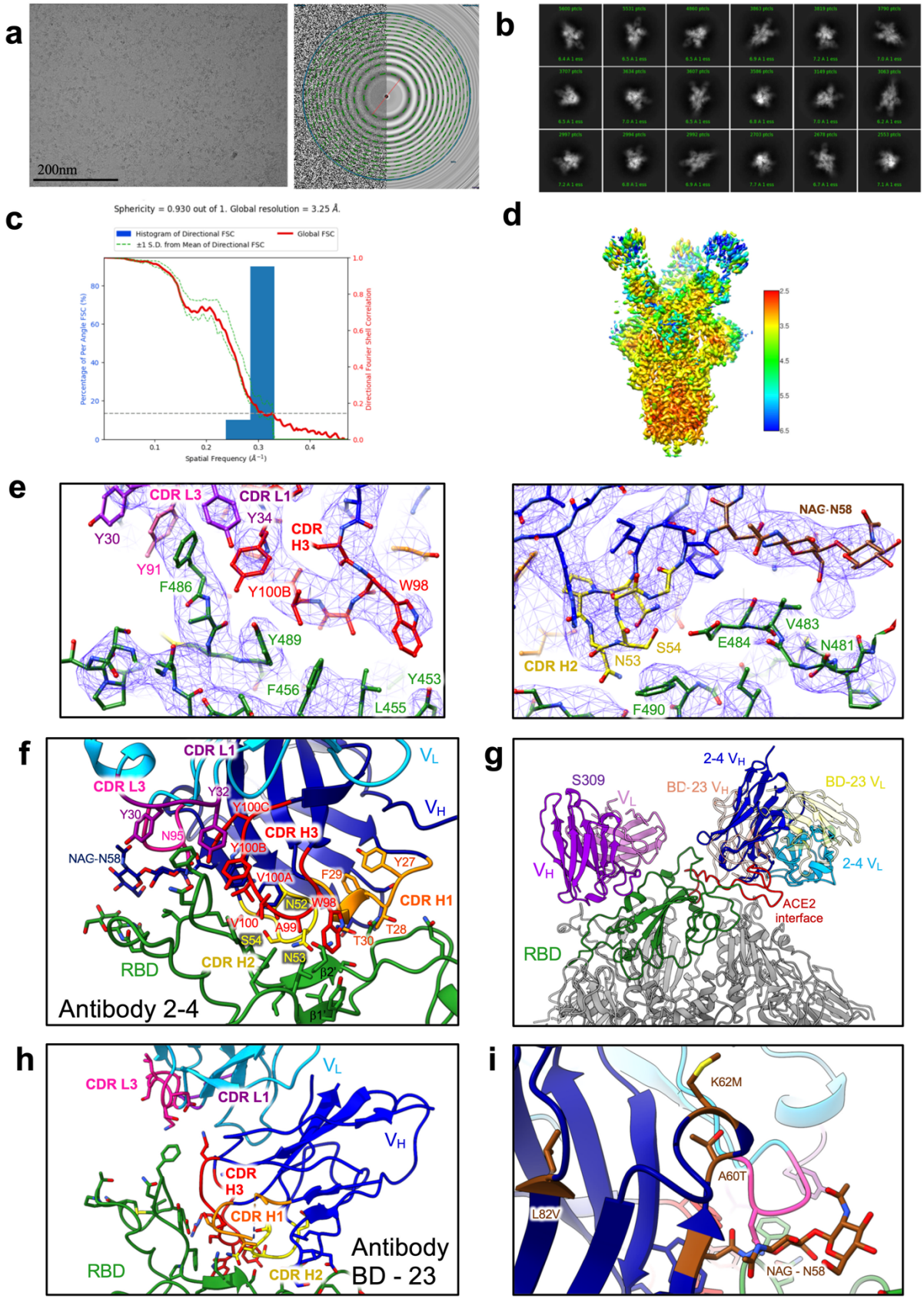
a
200nm
b
c
Sphericity = 0.930 out of 1. Global resolution = 3.25 Å.
Histogram of Directional FSC
Global FSC
±1 S.D. from Mean of Directional FSC
Percentage of Per Angle FSC (%)
Directional Fourier Shell Correlation
Spatial Frequency (Å⁻¹)
d
e
CDR L3
CDR L1
Y34
CDR H3
Y30
Y91
F486
Y100B
W98
Y489
F456
Y453
L455
NAG-N58
V483
E484
N481
S54
N53
CDR H2
F490
f
CDR L1
VL
CDR L3
Y32
Y100C
VH
Y30
N95
CDR H3
NAG-N58
Y100B
Y27
V100A
F29
CDR H1
N52
W98
V100
A99
T28
S54
T30
N53
RBD
CDR H2
β2
β1
Antibody 2-4
g
2-4 VH
S309
BD-23 VH
BD-23 VL
VL
VH
2-4 VL
ACE2
interface
RBD
h
CDR L3
VL
CDR L1
VH
CDR
H3
CDR H1
RBD
CDR H2
Antibody
BD - 23
i
K62M
A60T
L82V
NAG - N58

811 **Extended Data Fig. 7 Cryo-EM analysis of antibody 2-4 in complex with the S trimer. a,**
812 Representative micrograph and CTF of the micrograph. 8,324 micrographs were collected in total.
813 **b,** Representative 2D class averages. **c,** Resolution of the consensus map with C3 symmetry as
814 calculated by 3DFSC. **d,** The local resolution of the full map as calculated by cryoSPARC at an
815 FSC cutoff of 0.5. **e,** Representative density of the Fab 2-4 (blue) and RBD (green) interface,
816 showing interactions of CDR H3 in red, L1 in magenta, and L3 in light magenta (left), along with
817 CDR H2 and the N-linked glycosylation added by SHM at ASN58 (right). **f,** Fab 2-4 binding
818 interface with RBD. V_H is shown in blue, V_L in light blue, with CDRs H1 in orange, H2 in yellow,
819 H3 in red, L1 in magenta, and L3 in light magenta. **g,** Positions of antibodies 2-4, S309[8], and BD-
820 23[9] on the trimeric CoV-2 spike. **h,** Antibody BD-23[9] in complex with S trimer. **i,** Somatic
821 hypermutations found only in the antibody 2-4 heavy chain, shown in brown. The mutation A60T
822 creates an NxT sequence leading to N58 glycosylation.

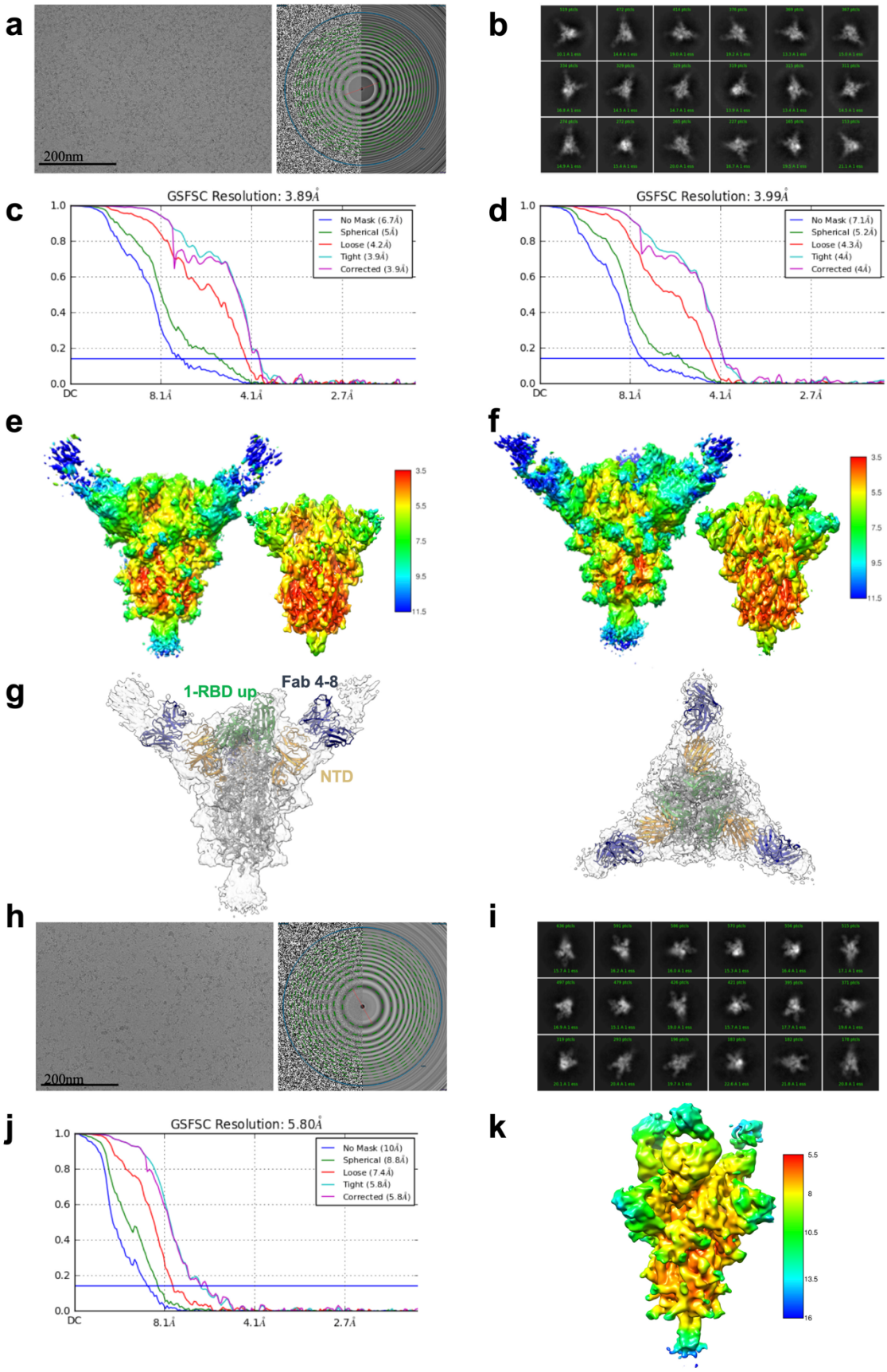
a
200nm
b
c
GSFSC Resolution: 3.89Å
No Mask (6.7Å)
Spherical (5Å)
Loose (4.2Å)
Tight (3.9Å)
Corrected (3.9Å)
DC
8.1Å
4.1Å
2.7Å
d
GSFSC Resolution: 3.99Å
No Mask (7.1Å)
Spherical (5.2Å)
Loose (4.3Å)
Tight (4Å)
Corrected (4Å)
e
f
g
1-RBD up
Fab 4-8
NTD
h
200nm
i
j
GSFSC Resolution: 5.80Å
No Mask (10Å)
Spherical (8.8Å)
Loose (7.4Å)
Tight (5.8Å)
Corrected (5.8Å)
k

824 **Extended Data Fig. 8 Cryo-EM data processing for antibodies 4-8 and 2-43 in complex with**
825 **S trimer. a,** Representative 4-8 micrograph and CTF of the micrograph. 3,153 micrographs were
826 collected in total. **b,** Representative 2D class averages. **c,** Resolution of the spike in the RBD down
827 conformation in complex with Fab 4-8. **d,** Resolution of the spike in the RBD up conformation in
828 complex with Fab 4-8. **e,** Local resolution of the spike in the RBD down conformation in complex
829 with Fab 4-8 at an FSC cutoff of 0.5, with two thresholds shown. **f,** Local resolution of the spike
830 in the RBD up conformation in complex with Fab 4-8 at an FSC cutoff of 0.5, with two thresholds
831 shown. **g,** Although the map was reconstructed at 4.0Å resolution, density for 4-8 Fab is poor due
832 to molecular motion. A rigid body fit with SARS-CoV-2 spike and an antibody variable domain
833 model is shown. **h-k,** Cryo-EM data processing for antibody 2-43 in complex with the S trimer. **h,**
834 Representative 2-43 micrograph and CTF of the micrograph. **i,** Representative 2D class averages.
835 **j,** Resolution of Fab 2-43 in complex with S trimer. **k,** The local resolution of the full map as
836 calculated by cryoSPARC at an FSC cutoff of 0.5.